

## Article

# Unsupervised Color-Based Flood Segmentation in UAV Imagery

Georgios Simantiris <sup>†</sup>  and Costas Panagiotakis <sup>\*,†</sup> 

Department of Management Science and Technology, Hellenic Mediterranean University,  
P.O. Box 128, 72100 Agios Nikolaos, Greece; ddk230@edu.hmu.gr

\* Correspondence: cpanag@hmu.gr

<sup>†</sup> These authors contributed equally to this work.

**Abstract:** We propose a novel unsupervised semantic segmentation method for fast and accurate flood area detection utilizing color images acquired from unmanned aerial vehicles (UAVs). To the best of our knowledge, this is the first fully unsupervised method for flood area segmentation in color images captured by UAVs, without the need of pre-disaster images. The proposed framework addresses the problem of flood segmentation based on parameter-free calculated masks and unsupervised image analysis techniques. First, a fully unsupervised algorithm gradually excludes areas classified as non-flood, utilizing calculated masks over each component of the LAB colorspace, as well as using an RGB vegetation index and the detected edges of the original image. Unsupervised image analysis techniques, such as distance transform, are then applied, producing a probability map for the location of flooded areas. Finally, flood detection is obtained by applying hysteresis thresholding segmentation. The proposed method is tested and compared with variations and other supervised methods in two public datasets, consisting of 953 color images in total, yielding high-performance results, with 87.4% and 80.9% overall accuracy and F1-score, respectively. The results and computational efficiency of the proposed method show that it is suitable for onboard data execution and decision-making during UAV flights.

**Keywords:** flood detection; image segmentation; remote sensing; unmanned aerial vehicle (UAV); unsupervised segmentation



**Citation:** Simantiris, G.; Panagiotakis, C. Unsupervised Color-Based Flood Segmentation in UAV Imagery. *Remote Sens.* **2024**, *16*, 2126. <https://doi.org/10.3390/rs16122126>

Academic Editors: Shuying Li and Michalis Savelonas

Received: 15 April 2024

Revised: 23 May 2024

Accepted: 8 June 2024

Published: 12 June 2024



**Copyright:** © 2024 by the authors. Licensee MDPI, Basel, Switzerland. This article is an open access article distributed under the terms and conditions of the Creative Commons Attribution (CC BY) license (<https://creativecommons.org/licenses/by/4.0/>).

## 1. Introduction

Natural disasters have historically exerted profound and far-reaching impacts on humanity. Recently, climate change has intensified weather phenomena, exacerbating the frequency and severity of natural disasters. Sudden and massive rainfall in mid-summer triggers devastating floods, while dry conditions paired with unseasonal strong winds ignite uncontrollable wildfires. Additionally, the occurrence of powerful earthquakes, volcanic eruptions, and hurricanes has surged. These disasters result in significant loss of life and property, disrupt essential services, such as water supply, electricity, and transportation, and pose serious health risks. The economic and psychological impacts on affected populations are enormous [1].

The extent of damage caused by natural disasters is heavily influenced by the readiness and risk reduction strategies of a region, which can vary significantly over time. Floods and hurricanes inflict the greatest damage. The spatial distribution of these disasters is uneven, with notable patterns in the relative distribution of disaster types and their occurrences across continents. Specifically, floods account for 32% of disasters, tropical storms for 32%, earthquakes for 12%, droughts for 10%, and other disasters for 14%. Geographically, Asia experiences the highest share at 38%, followed by the Americas at 26%, Africa and Europe each at 14%, and Oceania at 8% [2]. These statistics underscore the critical importance of tailored disaster preparedness and mitigation efforts across different regions.

Efforts to mitigate the impact of natural disasters include early warning systems, improved infrastructure resilience, disaster preparedness education, and international

cooperation for humanitarian assistance. Preparedness and response strategies are crucial to minimize the human toll and to facilitate faster recovery from such events. Natural disaster detection systems contribute to early warning, risk reduction, efficient resource allocation, and community preparedness. Using technology and global cooperation, these systems play a vital role in minimizing the impact of disasters on both human populations and the environment.

Technological advancements and collaborative technologies contribute to the sharing of disaster information benefiting from different types of media. Deep learning (DL) algorithms show promise in extracting knowledge from diverse data modalities, but their application in disaster response tasks remains largely academic. Systematic reviews have evaluated the successes, challenges, and future opportunities of using DL for disaster response and management [3], while also examining machine learning (ML) approaches [4], offering guidance for future research to maximize benefits in disaster response efforts. In this work, we specifically focus on flood segmentation. The relevant research undertaken is presented below, with a summary provided in Table 1.

**Table 1.** A brief overview of the research for this article, depicting approach (supervised, unsupervised), modality, and method.

Authors	Year	Approach	Imagery	Method
Chouhan, A. et al. [5]	2023	Supervised	Sentinel-1	Multi-scale ADNet
Drakonakis, G.I. et al. [6]	2022	Supervised	Sentinel-1, 2	CNN change detection
Dong, Z. et al. [7]	2023	Supervised	Sentinel-1	STANets, SNUNet, BiT
Hänsch, R. et al. [8]	2022	Supervised	HR satellite RGB	U-Net
He, Y. et al. [9]	2024	Weakly-supervised	HR aerial RGB	End-to-end WSSS framework structure constraints and self-distillation
Hernández, D. et al. [10]	2021	Supervised	UAV RGB	Optimized DNN
Hertel, V. et al. [11]	2023	Supervised	SAR	BCNN
Ibrahim, N. et al. [12]	2021	Semi-supervised	UAV RGB	RGB and HSI color models, k-means clustering, region growing
Inthizami, N.S. et al. [13]	2022	Supervised	UAV video	Improved ENet
Li, Z. et al. [14]	2023	Supervised	Sentinel-1	U-Net
Lo, S.W. et al. [15]	2015	Semi-supervised	RGB (Surveillance camera)	HSV color model, seeded region growing
Munawar, H.S. et al. [16]	2021	Supervised	UAV RGB	Landmark-based feature selection, CNN hybrid
Park, J.C. et al. [17]	2023	Supervised	HR satellite RGB	Swin transformer in a Siamese-UNet
Rahnemoonfar, M. et al. [18]	2021	Supervised	UAV RGB	InceptionNetv3, ResNet50, XceptionNet, PSPNet, ENet, DeepLabv3+
Şener, A. et al. [19]	2024	Supervised	UAV RGB	ED network with EDR block and atrous convolutions (FASegNet)
Shastri, A. et al. [20]	2023	Supervised	WorldView 2, 3 multispectral	CNN with atrous convolutions
Wang, L. et al. [21]	2022	Supervised	True Orthophoto (near infrared), DSM	Swin transformer and DCFAM
Wieland, M. et al. [22]	2023	Supervised	Satellite and aerial	U-Net model with MobileNet-V3 backbone pre-trained on ImageNet

Table 1. Cont.

Authors	Year	Approach	Imagery	Method
Bauer-Marschallinger, B. et al. [23]	2022	Unsupervised	SAR	Datacube, time series-based detection, Bayes classifier
Filonenko, A. et al. [24]	2015	Unsupervised	RGB (surveillance camera)	Change detection, color probability calculation
Landuyt, L. et al. [25]	2020	Unsupervised	Sentinel-1, 2	K-means clustering, region growing
McCormack, T. et al. [26]	2022	Unsupervised	Sentinel-1	Histogram thresholding, multi-temporal and contextual filters
Trombini, M. et al. [27]	2023	Unsupervised	SAR	Graph-based MRF segmentation

DL methods are increasingly applied to remote sensing imagery to address the limitations of traditional flood mapping techniques. Convolutional layer-based models offer improved accuracy in capturing spatial characteristics of flooding events, while fully connected layer-based models show promise when coupled with statistical approaches. Remote sensing analysis, multicriteria decision analysis, and numerical methods are replaced with DL models for flood mapping in which flood extent or flood inundation maps, susceptibility maps, and flood hazard maps determine, categorize, and characterize the disaster, respectively [28]. Furthermore, in a recent review, current DL approaches for flood forecasting and management are critically evaluated, highlighting their advantages and disadvantages. The challenges with data availability and potential future research directions are examined. The current state of DL applications in this area is fully evaluated, showing that they are a powerful tool to improve flood prediction and control [29].

Convolutional neural networks (CNNs) have proved to be effective in flood detection using satellite imagery. High-quality flood maps are generated with the help of temporal differences from various sensors after CNNs identify changes between permanent and flooded water areas using synthetic aperture radar (SAR) and multispectral images [6,7]. In addition, Bayesian convolutional neural networks (BCNNs) have been recommended to quantify the uncertainties associated with SAR-based water segmentation, because of their greater flexibility to learn the mean and the spread of the parameter posterior [11]. Also, a CNN employed to automatically detect inundation extents using the Deep Earth Learning, Tools, and Analysis (DELTA) framework demonstrated high precision and recall for water segmentation despite a diverse training dataset. Finally, the effects of surface obstruction due to the inability of optical remote sensing data to observe floods under clouds or flooded vegetation are quantified, suggesting the integration of flood models to improve segmentation accuracy [20].

The efficacy of CNNs in semantically segmenting water bodies in highly detailed satellite and aerial images from various sensors, with a focus on flood emergency response applications, is assessed by combining different CNN architectures with encoder backbones to delineate inundated areas under diverse environmental conditions and data availability scenarios. A U-Net model with a MobileNet-V3 backbone pre-trained on ImageNet consistently performed the best in all scenarios tested, while the integration of additional spectral bands, slope information from digital elevation models, augmentation techniques during training, and the inclusion of noisy data from online sources further improved model performance [22]. U-Nets and their variations have been widely used to tackle the problems of water bodies segmentation and flood extent extraction. In [14], another adjusted U-Net was proposed. With carefully selected parameters and training with pre-processed Sentinel-1 images for three-category classification, the proposed method was able to distinguish flood pixels from permanent water and background.

Since rapid damage analysis and fast coordination of humanitarian response during extreme weather events are crucial, flood detection, building footprint detection, and road network extraction have been integrated into an inaugural remote sensing dataset called SpaceNet 8 and a homonym challenge has been launched. The provided satellite

imagery posed real-world challenges, such as varying resolutions, misalignment, cloud cover, and lighting conditions. Top performing DL approaches focusing on multi-class segmentation showed that swiftly identifying flooded infrastructures, such as buildings and roads, can significantly shorten response times. Simple U-Net architectures yielded the best balance of accuracy, robustness, and efficiency, with strategies such as pre-training and data augmentation proving crucial to improve model performance [8].

In Ref. [13], an improved efficient neural network architecture (ENet) was the choice to segment the UAV video of flood disaster. The proposed method consists of atrous separable convolution as the encoder and depth-wise separable convolution as the decoder. In Ref. [5], a multiscale attentive decoder-based network (ADNet) designed for automatic flood identification using Sentinel-1 images outperformed recent DL and threshold-based methods when validated on the Sen1floods11 benchmark dataset. Through detailed experimentation on various dataset settings, ADNet demonstrated effective delineation of permanent water, flood water, and all water pixels using both co-polarization (VV) and cross-polarization (VH) inputs from Sentinel-1 images.

Transformers have also been successfully applied for semantic segmentation in remote sensing images. A novel transformer-based scheme employing the Swin Transformer as the backbone to better capture context information and a densely connected feature aggregation module (DCFAM) serving as a novel decoder to restore resolution and generate accurate segmentation maps proved to be effective in the ISPRS Vaihingen and Potsdam datasets [21]. An improved transformer-based multiclass flood detection model capable of predicting flood events while distinguishing between roads and buildings was introduced, which, with an additional novel loss function and a road noise removal algorithm, achieved superior performance, particularly in road evaluation metrics such as APLS [17]. Finally, the Bitemporal image Transformer (BiT) model scored highest in a change detection approach that better captures the changed region [7].

Dilated or atrous convolutions, which increase the network's receptive field and reduce the number of trained parameters needed [30], are utilized in an effort to speed up search and rescue operations after natural disasters, such as floods, high tides, and tsunamis. FASegNet, a novel CNN-based model featuring dilated convolutions, was specifically designed for flood and tsunami area segmentation. FASegNet utilizes encoder and decoder networks with an encoder-decoder-residual (EDR) block to effectively extract local and contextual information. An encoder-decoder high-accuracy activation cropping (EHAAC) module minimizes information loss at the bottleneck, and skip connections transfer information between the encoder and decoder networks, outperforming other segmentation models [19].

A novel weak training data generation strategy and an end-to-end weakly supervised semantic segmentation (WSSS) method, called TFCSD, challenges urban flood mapping [9]. By decoupling the acquisition of positive and negative samples, the weak label generation strategy significantly reduces the burden of data labeling, enabling quick flood mapping in emergencies. Additionally, the proposed TFCSD method improves edge delineation accuracy and algorithm stability compared to other methods, especially in emergency scenarios where pre-disaster river data are accessible, or when using the SAM ([31]) assisted interactive labeling method if such data are unavailable.

Satellites such as Sentinel-1 and Sentinel-2 play a key role in flood mapping due to their rapid data acquisition capabilities. Their effectiveness in mapping floods across Europe was evaluated in a study in which the results indicate that observation capabilities vary based on the size of the catchment area, and suggest that employing multiple satellite constellations significantly increases flood mapping coverage [32]. The urgent need for real-time flood management systems by developing an automated imaging system using unmanned aerial vehicles (UAVs) to detect inundated areas promptly is addressed, so that emergency relief efforts will not be hindered by current satellite-based imaging systems, which suffer from low accuracy and delayed response. By employing the Haar cascade classifier and DL



algorithms, a hybrid flood detection model combining landmark-based feature selection with a CNN demonstrated improved performance over traditional classifiers [16].

Specially designed datasets have been introduced to address the lack of high-resolution (HR) imagery relevant to disaster scenarios. In [18], FloodNet, a high resolution (HR) UAV imagery dataset, capturing post-flood damage, aims to detect flooded roads and buildings and distinguish between natural and flooded water. Baseline methods for image classification, semantic segmentation, and visual question are evaluated, highlighting its significance for analyzing disaster impacts with various DL algorithms, such as XceptionNet and ENet.

To facilitate efficient processing of disaster images captured by UAVs, an AI-based pipeline was proposed enabling semantic segmentation with optimized deep neural networks (DNNs) for real-time flood area detection based directly on UAVs, minimizing infrastructure dependency and resource consumption of the network. The experimental results confirmed the feasibility of performing sophisticated real-time image processing on UAVs using GPU-based edge computing platforms [10].

It becomes clear that DL methods offer improved segmentation by creating adaptive mapping relationships based on contextual semantic information. However, these methods require extensive manual labeling of large datasets and lack interpretability, suggesting the need to address these limitations for further progress. Traditional ML methods, on the other hand, rely on manually designed mappings. Systematic reviews of water body segmentation over the past 30 years examine the application and optimization of DL methods and outline traditional methods at both pixel and image levels [33]. Evaluating the strengths and weaknesses of both approaches prompts a discussion of the importance of maintaining knowledge of classical computer vision techniques. There remains value in understanding and utilizing these older techniques. The knowledge gained from traditional computer vision (CV) methods can complement DL, expanding the available solutions. There also exist scenarios in which traditional CV techniques can outperform DL or be integrated into hybrid approaches for improved performance. Furthermore, traditional CV techniques have been shown to have benefits, such as reducing training time, processing, and data requirements compared to DL applications [34].

In 2015, a method for automatically monitoring flood events in specific areas was proposed using remote cyber-surveillance systems and image-processing techniques. When floods are treated as possible intrusion objects, the intrusion detection mode is utilized to detect and verify flood objects, enabling automatic and unattended flood risk level monitoring and urban inundation detection. Compared to large-area forecasting methods, this approach offered practical benefits, such as flexibility in location selection, no requirement for real-world scale conversion, and a wider field of view, facilitating more accurate and effective disaster warning actions in small areas [15]. Real-time methods to detect flash floods using stationary surveillance cameras, suitable for both rural and urban environments, have become quite popular. Another method used background subtraction to detect changes in the scene, followed by morphological closing to unite pixels belonging to the same objects. Additionally, small separate objects are removed, and the color probability is calculated for the foreground pixels, filtering out components with low probability values. The results are refined using the edge density and boundary roughness [24].

Unsupervised object-based clustering was also used for flood mapping in SAR images. The framework segments the region of interest into objects, converts them into a SAR optical feature space, and clusters them using K-means, with the resulting clusters classified based on centroids and refined by region growing. The results showed improved performance compared to pixel and object-based benchmarks, with additional SAR and optical features enhancing accuracy and post-processing refinement reducing sensitivity to parameter choice even in difficult cases, including areas with flooded vegetation [25]. The same techniques were also proposed for flood detection purposes in UAV-captured images. Employing RGB and HSI color models and two segmentation methods, K-means clustering

and region growing, in a semi-supervised scheme, showed potential for accurate flood detection [12].

There is also a datacube-based flood mapping algorithm that uses Sentinel-1 data repetition and predefined probability parameters for flood and non-flood conditions [23]. The algorithm autonomously classifies flood areas and estimates uncertainty values, demonstrating robustness and near-real-time operational suitability. It also contributed to the Global Flood Monitoring component of the Copernicus Emergency Management Service.

Contextual filtering on multi-temporal SAR imagery resulted in an automated method for mapping non-urban flood extents [26]. Using tile-based histogram thresholding refined with post-processing filters, including multitemporal and contextual filters, the method achieved high accuracy. Additionally, confidence information was provided for each flood polygon, enabling stable and systematic inter-annual flood extent comparisons at gauged and ungauged sites.

Finally, in [27], an unsupervised graph-based image segmentation method was proposed that aims to achieve user-defined and application-specific segmentation goals. This method utilizes a graph structure over the input image and employs a propagation algorithm to assign costs to pixels based on similarity and connectivity to reference seeds. Subsequently, a statistical model is estimated for each region, and the segmentation problem is formulated within a Bayesian framework using probabilistic Markov random field (MRF) modeling. Final segmentation is achieved through minimizing an energy function using graph cuts and the alpha-beta swap algorithm, resulting in segmentation based on the maximum a posteriori decision rule. In particular, the method does not rely on extensive prior knowledge and demonstrates robustness and versatility in experimental validation with different modalities, indicating its potential applicability across different domains. It was also successfully applied on SAR images for flood mapping.

Our review of related literature reveals a prevailing preference for supervised methodologies in contemporary applications, as they are utilized more frequently than unsupervised approaches (see Table 1). Additionally, there is a preference for satellite radar imagery due to its greater availability. Among the unsupervised methods, we identified only one that processes RGB images. However, this method depends on change detection, necessitating the availability of pre-disaster images.

In this paper, we propose a novel unsupervised method for flood segmentation utilizing color images acquired from UAVs. Without the need of large datasets, extensive labeling, augmentation, and training, the segmentation can be performed directly on the UAV deployed over the disaster area. Therefore, relief efforts can be swiftly directed to damaged sites, avoiding time loss, which can be crucial in saving lives and properties. Initially, we employ parameter-free calculated masks over each component of the LAB colorspace, utilizing as well an RGB vegetation index and the detected edges of the original image in order to provide an initial segmentation. Next, unsupervised image analysis techniques, such as distance transform, are adapted to the flood detection problem, producing a probability map for the location of flooded areas. Then, the hysteresis thresholding segmentation method is applied, resulting in the final segmentation. The main contributions of our work can be summarized as follows:

- *Novelty in Approach:* To our knowledge, this is the first fully unsupervised method for flood area segmentation in color images captured by UAVs. Our work addresses flood segmentation using parameter-free calculated masks and unsupervised image analysis techniques without any need for training.
- *Probability Optimization:* Flood areas are identified as solutions to a probability optimization problem, with an isocontour evolution starting from high-confidence areas and gradually growing according to the hysteresis thresholding method.
- *Robust Algorithm:* The proposed formulation results in a robust, simple, and effective unsupervised algorithm for flood segmentation.

- *Dataset Categorization:* We have introduced a dataset categorization according to the depicted scenery and camera rotation angle, into rural and urban/peri-urban, and no sky and with sky, respectively.
- *Efficiency and Real-Time Processing:* The framework is efficient and suitable for on-board execution on UAVs, enabling real-time processing and decision-making during flight. The processing time per image is approximately 0.5 s, without the need for pre-processing, substantial computational resources, or specialized GPU capabilities.

These contributions highlight the novelty and effectiveness of our method, particularly its suitability for rapid and efficient deployment in disaster response scenarios.

The proposed system has been tested and compared with various variants of our own method, as well as with supervised approaches, using the Flood Area dataset introduced in [35], which consists of 290 color images. Our research did not identify other relevant unsupervised methodologies, and the proposed system yielded high-performance results. Additionally, experimental results of the proposed method are reported on the Flood Semantic Segmentation dataset [36], which comprises 663 color images.

The rest of this paper is organized as follows: Section 2 introduces the datasets used for this article. Section 3 presents our proposed unsupervised methodology. The experimental results and a comprehensive discussion are given in Section 4. Finally, conclusions and consideration of future work are provided in Section 5.

## 2. Materials

We employed two publicly available datasets for this study to demonstrate the robustness and general applicability of our method. First, the dataset used to assess the efficacy of our approach and facilitate comparative analyses with alternative methodologies is called Flood Area, consisting of color images acquired by UAVs and helicopters [35]. It contains 290 RGB images depicting flood hit areas, as well as their corresponding mask images with the water region segmentations. The ground truth images were annotated by the dataset creators using Label Studio, an open-source data-labeling software. The images were downloaded selectively from the Internet; thus, the dataset exhibits a wide range of image variability, depicting urban, peri-urban, rural areas, greenery, rivers, buildings, roads, mountains, and the sky. Furthermore, there are image acquisitions relatively close to the ground as well as from a very high altitude and from diverse camera rotation angles around the X-axis (roll) and Y-axis (pitch). If pitch and roll are zeros, this means that the camera is looking down (top-down view). Hereafter, we use the term “camera rotation angle” to present the angle between the current view plane and the horizontal plane (top-down view). The images have different resolutions and dimensions with height and width ranging from 219 up to 3648 and 330 up to 5472, respectively. Representative images with their corresponding ground truths are shown in Figure 1.



**Figure 1.** Sample images from the Flood Area dataset (top) and their corresponding ground truths (bottom).

Second, to confirm the universal functionality of our approach, we employed the Flood Semantic Segmentation Dataset [36]. It consists of 600 and 63 color images for training and validation, respectively. Since our method is fully unsupervised, it does not require training, and, therefore, we used all 663 images for evaluation. Similarly to the initial dataset, this dataset comprises images obtained from UAVs, accompanied by their respective ground truth annotations, portraying diverse flooded scenes captured from various camera perspectives. The image sizes and resolutions also vary, but were all resized and, if necessary, zero-padded, to  $512 \times 512$  by the creator, as shown in Figure 2.



**Figure 2.** Sample images from the Flood Semantic Segmentation dataset (**top**) and their corresponding ground truths (**bottom**).

### 3. Methodology

#### 3.1. System Overview

We propose an approach which gradually removes image areas classified as non-flood, based on binary masks constructed from color and edge information. Our method is fully unsupervised, meaning that there is no training process involved, and thus no need of ground truth labeling. We use the labels provided by the datasets only for evaluation purposes of our method. A repetitive process, consisting of the same algorithmic steps, is applied over each of the components extracted from the color image in order to identify areas that are not affected by floods. For each component, as described below, a binary map is obtained in which areas identified as non-flood are discarded, leading to a final mask of potential flood areas (PFAs), refined by simple morphological operations. The flood's dominant color is calculated by weighting the potential flood area pixels and hysteresis thresholding yields the final segmentation. An overview of our proposed methodology is graphically depicted in Figure 3. In the following, we analytically present the proposed methodology.



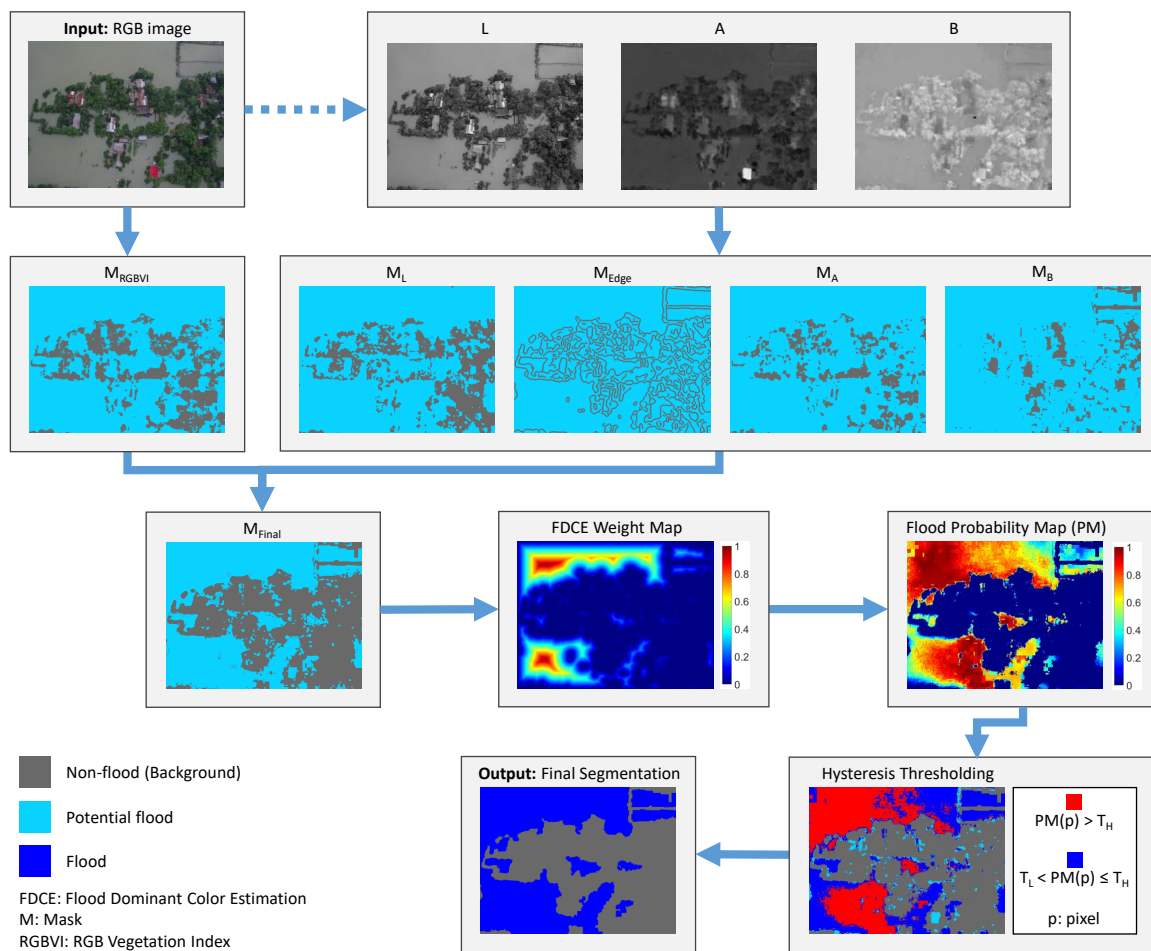


**Figure 3.** Overview of the proposed approach.

### 3.2. RGB Vegetation Index Mask

In both urban and rural areas, the landscape is lush with greenery, largely attributed to the abundant presence of trees and vegetation. Since trees are unlikely to be fully covered by flood events, our first concern is to rule out the greenery, noticing also in our experiments that, using only a flood color approach, vegetation is more likely to be misclassified as flood water. Therefore, we use the RGB Vegetation Index (RGBVI), introduced in [37]. This index was successfully applied in [38] as a first step in detecting and counting trees using region-based circle fitting. RGBVI particularly improves sensitivity to vegetation characteristics while mitigating the impact of interfering factors, such as reflection of the background soil and directional effects. However, as shown in Equation (1), it can be influenced by the color quality of the image, e.g., due to bad atmospheric conditions by the time of the image acquisition. It is defined as the normalized difference between the squared green reflectance and the product of blue and red reflectance:

$$RGBVI = \frac{(R_G)^2 - (R_B \times R_R)}{(R_G)^2 + (R_B \times R_R)} \quad (1)$$

where  $R_R$ ,  $R_B$ , and  $R_G$  denote the red, blue, and green reflectance, respectively. In Ref. [39], the authors, after extensive experimentation, concluded that an RGBVI value of 0.15 is optimal for greenery detection. In this work, we preferred to set a stricter value, e.g., 0.2, so that any value exceeding this threshold is characterized as greenery and, therefore, is not flooded, resulting from the  $M_{RGBVI}$  mask. The threshold is essentially a constant applicable to any color image input. A stricter value ensures the detection of only confident green



areas. Consequently, if the floodwaters also exhibit green hues, they will not be selected, as the mixture of vegetation and water results in a lighter color compared to the actual vegetation. With this mask, we are able to rule out a large number of image pixels, since visible vegetation cannot be flooded. Particularly in the Flood Area dataset in some images depicting rural areas, up to 92.8% of pixels can be characterized as greenery, and thus non-flood, while, on average, over the whole dataset, 17.94% of pixels are ruled out this way (median value is 14.16%). The binary image produced from this process results in a set of pixels definitively classified as non-flood, leaving the remaining pixels as ambiguous. This ambiguous region is referred to as the potential flood area (PFA). Within this area, using the modules described below, certain pixels will be classified and segmented as flood, while the others will be excluded.

In Figure 4, examples of RGBVI masks are shown for (a) urban and (b) rural areas from the Flood Area dataset, where the dim gray color corresponds to the detected greenery. We can clearly notice that, especially in rural areas, a substantial number of image pixels are rightly characterized as trees and vegetation, and, therefore, these areas cannot be flooded. This technique also works in urban areas where vegetation is present. But there are also cases where the RGB Vegetation Index is not quite efficient, especially when the image color quality is poor due to the camera rotation angle and/or weather conditions (Figure 4c).

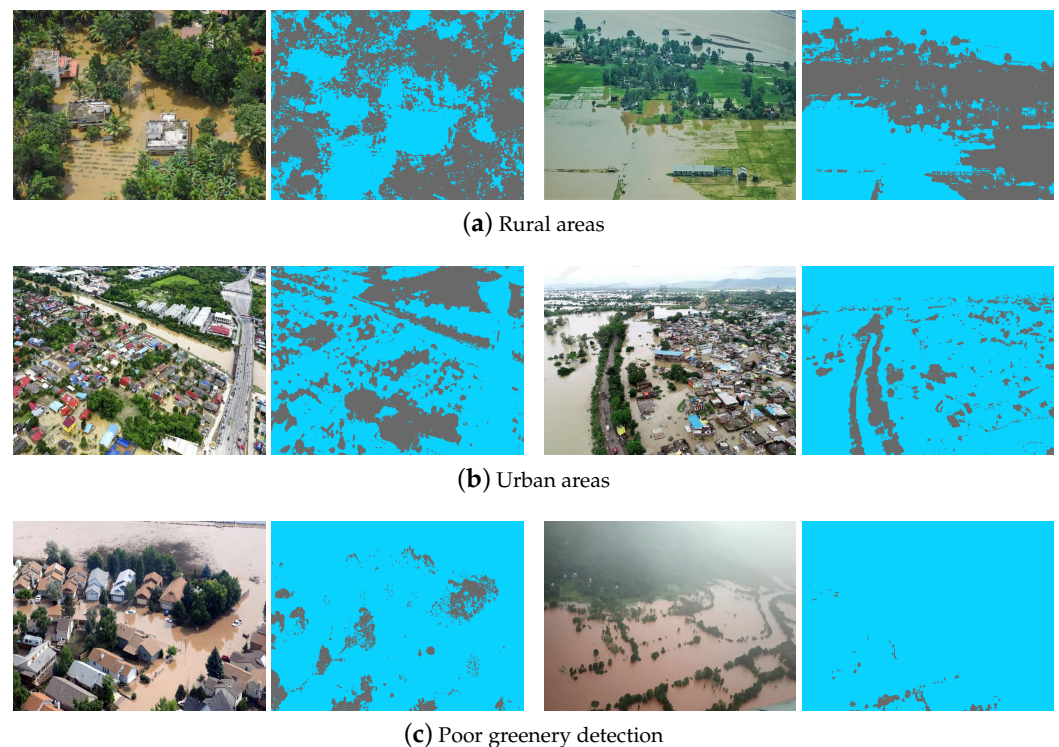


**Figure 4.** The original images (from the Flood Area dataset) and the corresponding RGBVI masks on their right side. The masks show detected greenery with dim gray color. Examples are presented for (a) urban areas, (b) rural areas, and (c) poor or failed greenery detection. The remaining potential flood areas are shown in cyan.

### 3.3. LAB Components Masks

The LAB color space offers several advantages over the RGB color space, such as perceptual uniformity, wide color gamut, separation of color and lightness, and robustness to illumination [40]. The LAB color space is designed to be perceptually uniform, which means that a small change in the LAB values corresponds to a similar perceptual change in color across the entire color space, making it more suitable for color-based applications where accurate perception of color differences is important. It encompasses a wider range of colors compared to the RGB color space, particularly in terms of the human perceptual color

space. This allows for a more accurate representation of colors that fall outside the RGB gamut. The LAB color space is less affected by changes in illumination compared to the RGB color space, since lightness is a separate component. This separation is advantageous when independent control over lightness and color is desired, making it more suitable for applications where lighting conditions vary significantly [41]. Considering that the LAB color space offers greater flexibility and accuracy in color representation and manipulation compared to the RGB color space, and since, in our application, precise color information is critical, we selected the CIE 1976 L\*a\*b\* color space, commonly known as CIELAB [42]. Subsequently, we convert the image to the CIELAB color space for further processing, following the methodology described in [43].

Using the L, A, and B components, we derive three more masks, where areas can potentially be characterized as non-flood, exploiting the standard deviation values of the data relative to their central tendency for each color component. In flooded areas, the value of each color component in the LAB color space is usually higher than the corresponding values of the background. So, we select a lower threshold  $\Delta_C$ ,  $C \in \{L, A, B\}$  to create binary masks that detect regions probably belonging to non-flood areas.  $\Delta_C$  is calculated by subtracting the standard deviation ( $\sigma_C$ ) from the mean value ( $\mu_C$ ) over each color component (C) of the LAB color space:

$$\Delta_C = \mu_C - \sigma_C, \quad C \in \{L, A, B\} \quad (2)$$

Figure 5 shows the average value of (a) L, (b) A, and (c) B color components computed on flood (blue curve) and background (red curve) pixels for each image of the Flood Area dataset, sorted in ascending order. The yellow curves represent the corresponding threshold  $\Delta_C$  used to create the three masks. Since flooded areas have elevated values observed in each component of the LAB color space, each mask  $M_L$ ,  $M_A$ , and  $M_B$  is labeled as non-flood, when the component's pixel value is smaller than  $\Delta_C$ . Because the two classes (flood and non-flood) have very similar characteristics, setting a threshold between them makes distinguishing the classes challenging. The proposed equation for  $\Delta_C$  is designed to produce a threshold that classifies pixels with values significantly below the flood, so that non-flood pixels can be excluded with high confidence. The objective is not to distinguish between the two classes, but rather to provide an initial segmentation by excluding pixels that do not belong to the flood class. In the Flood Area dataset, we observed that the median value, computed over all images in the dataset, of the percentage of pixels that belong to the non-flood class according to the mask  $M_L$ ,  $M_A$  and  $M_B$  is only 2.3%, 1.3%, and 2.0%, respectively. This means that the  $M_L$ ,  $M_A$ , and  $M_B$  masks have a very low number of wrong-classified flood pixels, providing a robust initial segmentation for our method.

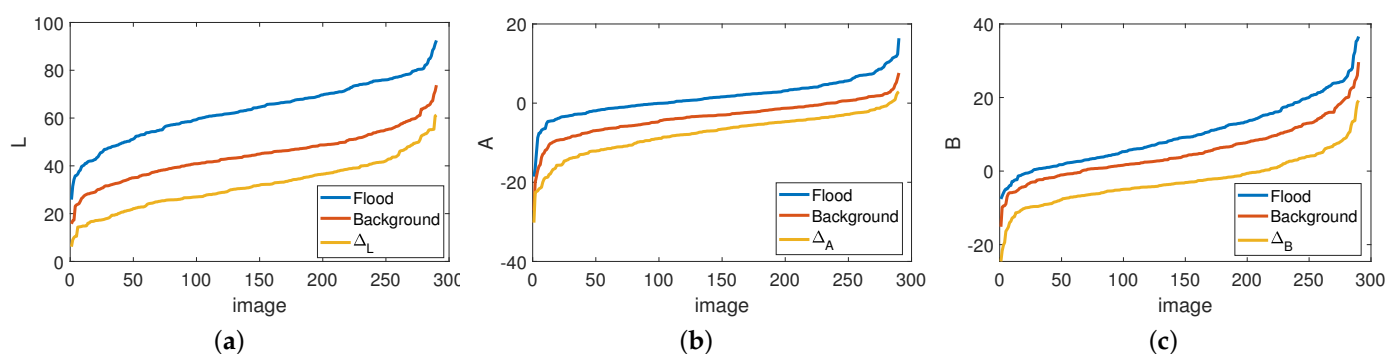


**Figure 5.** Blue and red curves correspond on the average value of (a) L, (b) A, and (c) B color components computed on flood and background pixels, respectively, for each image of the Flood Area dataset, sorted in ascending order. The yellow curves show the corresponding  $\Delta_C$  threshold.

Edges often correspond to significant changes in intensity or color in an image. Detecting these edges allows for the extraction of important features, such as object boundaries, contours, and shapes, which are essential for further analysis and interpretation of image content. Identifying edges helps in highlighting important structures and details and serves as a fundamental step in image segmentation, which involves partitioning an image into regions with similar characteristics. Edges act as boundaries between different regions, which makes them essential for accurate segmentation and analysis of image content [44]. It is clear that edges can be useful to locate borders between flooded and non-flooded areas and should, therefore, be excluded from the flood water class. To acquire the fifth mask,  $M_{Edge}$ , the L component is initially smoothed using a 2-D Gaussian kernel with a standard deviation of 4. Subsequently, the Canny edge detection algorithm is applied to the blurred L component, resulting in dilated edges. These edge pixels are then designated as non-flood areas. The  $M_{Edge}$  mask is also useful, because by detecting the borders of small objects (e.g., buildings, cars, trees, etc.), then the weights of their nearby pixels are reduced in the flood-dominant color estimation, increasing the robustness of the estimation (see Section 3.4).

Examples from the Flood Area dataset of the four LAB component masks  $M_L$ ,  $M_A$ ,  $M_B$ , and  $M_{Edge}$  are depicted in Figure 6. We observe that each color component and the detected edges contribute to further classifying image pixels as background (with dim gray color), thus excluding them from potential flood areas (cyan color). Non-flood areas are strengthened, when so classified by multiple components, but also complemented by being detected by one component when others failed to do so. For the whole Flood Area dataset, on average 25.43%, 27.75%, 29.82%, and 7.45% of pixels, respectively, for the L, A, and B component, and the edge image, are classified as non-flood. Notice the sky in the first image of Figure 6, detected only by the B component as non-flood, and the hillside in the second image, which as a non-flood area is strengthened by all components. In any case, the borders of small objects are well detected by the  $M_{Edge}$  mask, increasing the robustness of the flood-dominant color estimation, which is described in the next subsection.

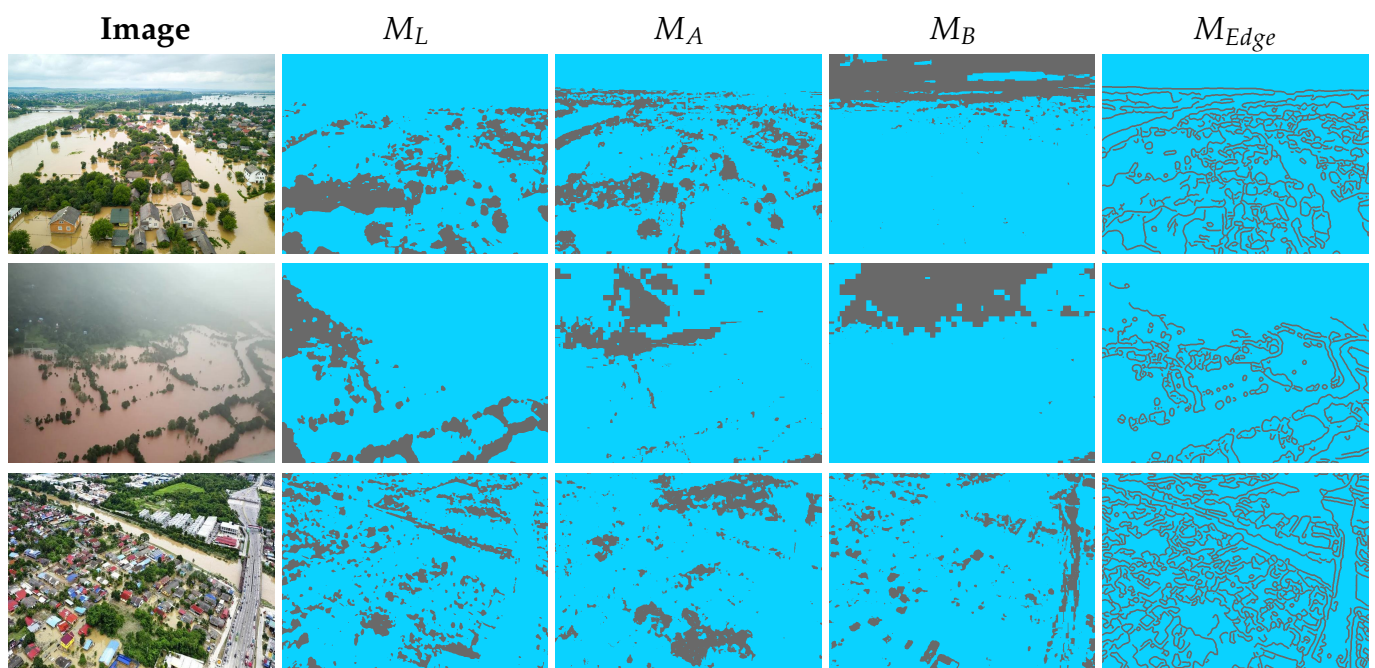


**Figure 6.** Original images from the Flood Area dataset and their corresponding LAB components masks  $M_L$ ,  $M_A$ ,  $M_B$ , and  $M_{Edge}$  from left to right. Note that the edges in  $M_{Edge}$  are dilated for illustration purposes. Non-flood areas are depicted with dim gray color, whereas remaining potential flood areas are shown in cyan.

### 3.4. Flood Dominant Color Estimation

As described in Sections 3.2 and 3.3, five masks with potential non-flooded areas are constructed. There are cases where these masks describe approximately the same areas, but essentially the masks complement each other. When all masks are robust in classifying an area as non-flood, then the conclusion for this specific area is strengthened. But if one mask is weak in characterizing the area as non-flood, the other masks function as reinforcement. The final mask ( $M_{Final}$ ) for the non-flood class is derived by combining these individual masks, as also depicted in Figure 3:

$$M_{Final} = M_{RGBVI} \cup M_L \cup M_A \cup M_B \cup M_{Edge} \quad (3)$$

The morphological operation of image closing follows, merging adjacent areas that are partially separated and connecting nearby regions. Excluding the non-flood labeled pixels of the final mask leaves us with potential flood areas, which, of course, have to be refined, as described below.

We opt for a weighted approach to estimate the dominant color of the flood in the image. The rationale behind this approach is that we obtain a set of confidently non-flood areas through the union of five binary masks. All other regions in the image are designated as potential flood areas. Within these PFAs, the objective is to identify the dominant color of the flood for precise segmentation. The likelihood that a pixel belongs to a flood area increases with its distance from a non-flood area. Consequently, such pixels should have a greater influence on the estimation of the dominant color, achieved by assigning them a higher weight. Taking into account the non-flood area derived from  $M_{Final}$ , the Euclidean distance transform [45] assigns to each potential flood pixel a value representing its distance to the nearest boundary pixel (non-flood). This representation of the spatial relationship between the pixels serves as a weight map ( $W$ ), where the pixels farther away from non-flood areas receive greater weights such that their color ( $I_C$ ) will exert a more significant influence on the process of the flood's dominant color estimation:

$$W(p) = \begin{cases} \frac{\|p-p'\|}{\max_{q \in PFA} \|q-q'\|} & , \text{ if } p \in PFA \\ 0, & \text{ otherwise} \end{cases} \quad (4)$$

where  $\|.\|$  denotes the Euclidean norm,  $p$  is the pixel for which the weight value is calculated, and  $p'$  is the nearest non-flood pixel to  $p$ . Similarly,  $q'$  is the nearest non-flood pixel to  $q \in PFA$ . The denominator in Equation (4) is used for normalization purposes so that  $W(p) \leq 1$ .

The weighting variance ( $\sigma_C^2$ ) for each color component ( $C$ ) is calculated on the potential flood area ( $PFA$ ) as follows:

$$\sigma_C^2 = \frac{N}{N-1} \cdot \frac{\sum_{p \in PFA} W(p) \cdot (I_C(p) - \mu_C)^2}{\sum_{p \in PFA} W(p)} \quad (5)$$

where  $N$  and  $p$  are the total amount of potential flood area pixels and an image pixel, respectively. The mean color value of the potential flood for each component  $C \in L, A, B$  is represented by  $\mu_C$ :

$$\mu_C = \frac{\sum_{p \in PFA} W(p) \cdot I_C(p)}{\sum_{p \in PFA} W(p)} \quad (6)$$

The estimated variance ( $\sigma_C^2$ ) can be much higher than the real one, due to the fact that  $PFA$  may also contain non-flood pixels. Furthermore, the estimated  $\sigma_C^2$  in the  $PFA$  region should be much lower than the corresponding variance estimated in the entire image ( $\overline{\sigma_C^2}$ ), due to the high color similarity between the flood pixels. So,  $\sigma_C^2$  is corrected to a predefined percentage (e.g., 20%) of  $\overline{\sigma_C^2}$  when it exceeds this value.



In this work, the probability for potential flood area pixels over each color component is defined in Equation (7) via the exponential component of the normal probability distribution function (Gaussian kernel) that is ranged in  $[0, 1]$ :

$$P_C(p) = e^{-\frac{(I_C(p) - \mu_C)^2}{2\sigma_C^2}} \quad (7)$$

The decisive probability map ( $PM$ ) is then constructed, as shown in Equation (8),

$$PM(p) = \left( P_L(p) \sqrt{P_A(p)} \sqrt{P_B(p)} \right)^{\frac{4}{7}} \quad (8)$$

accounting for the greater significance of the  $L$  component with exponent term one. This is because water reflects more light than most backgrounds (excluding the sky), significantly affecting the luminance captured in the  $L$  component of the LAB color space. The component  $A$  has the second significance, with an exponent term equal to  $\frac{1}{2}$ . The component  $B$  is the least significant, with an exponent term equal to  $\frac{1}{4}$ . In Equation (8), the exponent term  $\frac{4}{7}$  is used for normalization purposes, giving the sum of exponent terms one. The use of different exponent terms on the three color components slightly improves the results of the proposed method, as shown in Table 3. We achieved 0.5% and 0.3% higher F1-score ( $F_1$ ), compared to the version of the system having equal significance to all color components (see Equation (9)) and equal significance to the  $A$  and  $B$  color components (see Equation (10)), respectively.

$$PM_{eqLAB}(p) = (P_L(p)P_A(p)P_B(p))^{\frac{1}{3}} \quad (9)$$

$$PM_{eqAB}(p) = \left( P_L(p) \sqrt{P_A(p)P_B(p)} \right)^{\frac{1}{2}} \quad (10)$$

Figure 7 illustrates examples of probability maps derived after the corresponding initialization masks and weight maps for examples from the Flood Area dataset. In fact, potential flood areas (cyan color) have a higher probability (red color) compared to the background. Areas classified as non-flood (dim gray color) by Equation (3) exhibit zero weights and probabilities (dark blue color) such that they will not contribute to the flood's dominant color estimation. However, when the flood's color is equivalent to the color of background areas, which were not eliminated by the masks used to initialize our method (see Sections 3.2 and 3.3), there can be the case of high probabilities turning up in non-flood areas, as depicted in the example in the last row, where parts of the road exhibit a tendency towards flood.

At this point, using a single threshold value on the decisive probability map to perform the final segmentation can lead to quite satisfactory results (see Table 3, row UFS-REM). However, we opted for dual thresholds, as described in the following subsection.



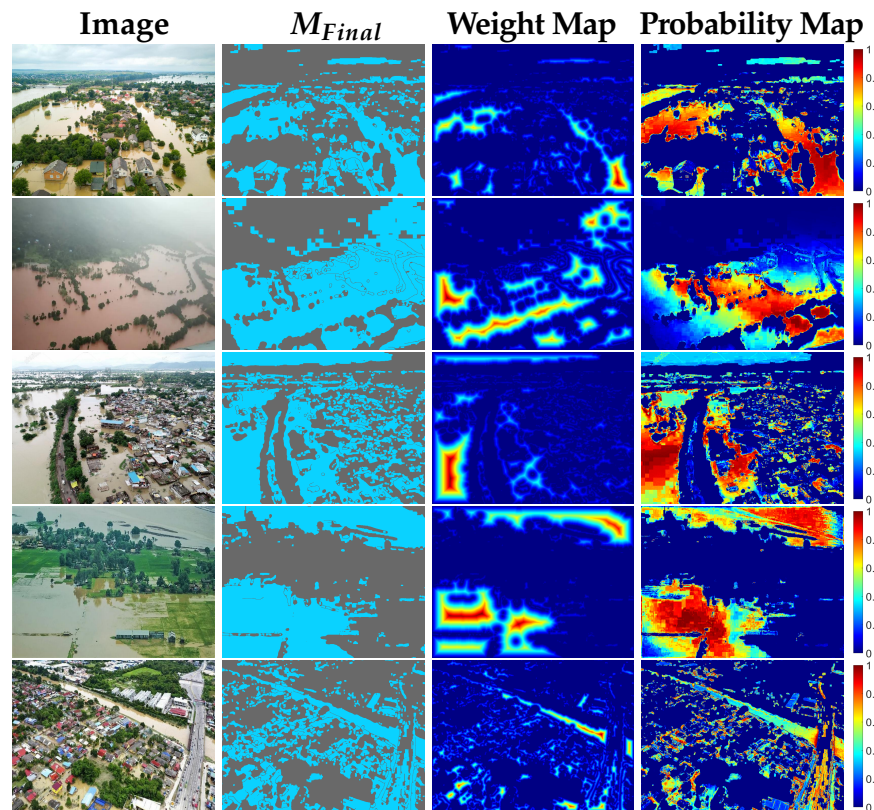


**Figure 7.** Probability maps (column 4) obtained using potential flood areas of  $M_{Final}$  (column 2), weight maps (column 3), as generated by the distance transform and the corresponding images from the Flood Area dataset (column 1). Potential flood area is shown in cyan, and non-flood area in dim gray color. The weights and probabilities range from 0 (dark blue color) to 1 (red color).

### 3.5. Hysteresis Thresholding

The probability map provides a good indication of the location of flooded areas. This now defines a probability optimization problem. To proceed to the final decision, we preferred two different threshold values to distinguish between actual flood and background. The isocontour evolves starting from the high-confidence areas and gradually grows to segment the flooded area. This technique is known as hysteresis thresholding and was first implemented for edge detection [44]. The main steps of the hysteresis thresholding method are described below:

- We adapt the process for region growing, where the high threshold  $T_H$  is applied to the entire probability map to identify pixels with  $PM(p) > T_H$  as flood (strong flood pixels). These regions have high confidence to belong to flood areas, so they can be used as seeds in a region-growing process that is described below.
- Next, a connectivity-based approach is used to track the flood. Starting from the pixels identified in the first step, the algorithm looks at neighboring pixels. If a neighboring pixel has a probability value higher than the low threshold  $T_L$  (weak flood pixel), it is ultimately considered part of the flood.
- This process continues recursively until no more connected pixels above the low threshold are found.

The hysteresis effect prevents the algorithm from being too sensitive to small fluctuations in probability. Pixels that fall between the low and high thresholds, but are not directly connected to strong flood pixels, are not considered flood. However, if a weak flood pixel is connected to a strong flood pixel, it is still considered to be part of the flood. In this way, flood continuity is maintained and false detections are reduced, so that flood boundaries are accurately identified.

We have set the low and high thresholds to be at the 1% and 75% marks, respectively. This means that pixels with a probability greater than 75% are directly classified as flood, while pixels with a probability equal or less than 1% are directly classified as non-flood. The rest of the pixels  $p$  with  $PM(p) \in (0.01, 0.75]$  fall into a substantial margin of uncertainty regarding their classification as flood pixels. This uncertainty is ultimately reduced when these pixels are connected to strongly classified flood pixels. Essentially,  $T_H$  and  $T_L$  are the only parameters which could be defined exclusively by the user. But, as we can observe in Figure 12, any value in the vicinity of  $T_L = 0.01$  and  $T_H = 0.75$  does not change the outcome substantially, thus making our methodology robust.

In Figure 8, the middle column shows the hysteresis thresholding process for four images of the Flood Area dataset in the second column. For the whole set of potential flood areas, red-colored pixels are those with probability greater than  $T_H$  and, therefore, certain to belong to the flood class, while the blue-colored pixels have a probability in the range  $PM(p) \in (T_L, T_H]$ . For the latter, the flood class inclusion is guaranteed only when they are linked with red pixels. Cyan-colored pixels belong to PFAs but fall below the lower threshold, and, therefore, they will be assigned to the background class. The non-flood areas, according to the  $M_{Final}$  mask, are colored with dim gray pixels.

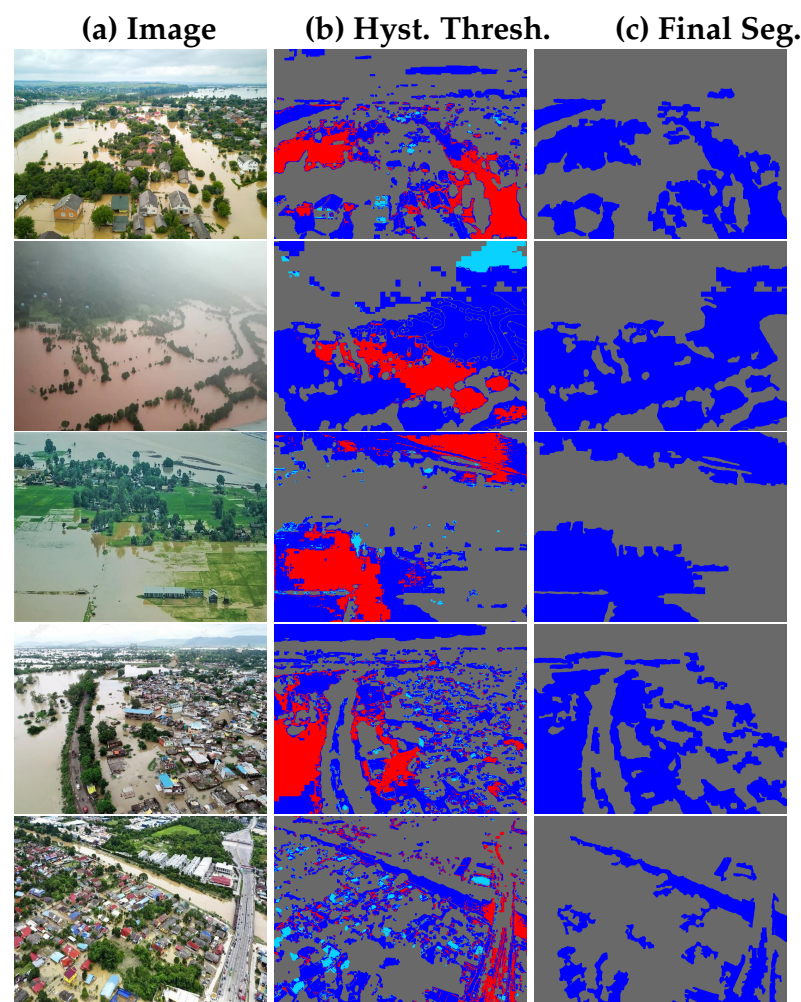


**Figure 8.** (a) Original image from the Flood Area dataset, (b) the applied hysteresis thresholding on the decisive probability map of the potential flood area, and (c) the final segmentation mask. (b) In red and blue are the pixels with  $PM(p) > T_H$  and  $T_L < PM(p) \leq T_H$ , respectively. Cyan-colored pixels are with  $PM(p) \leq T_L$ , they do not surpass the lower threshold, and are subsequently classified as background. The non-flood areas, according to the  $M_{Final}$  mask, are colored with dim gray pixels. (c) The last column shows the final segmentation obtained from our proposed method, where the flood is in blue and the background is in dim gray color.

### 3.6. Final Segmentation

The proposed methodology is completed by obtaining the final segmentation after the hysteresis thresholding is applied to the decisive probability map. For the derived flood areas, an edge correction is performed via the image dilation operation. The connected components of flood and non-flood areas are calculated, and relatively small areas are removed. In particular, if a blob is considered to be flooded but does not exceed about 0.3% of the whole image pixels, then this blob is reclassified as background to reduce noise effects, e.g., small water pits which do not belong to the flood area. Furthermore, background blobs with an area of 0.05% of all the pixels in the image are attributed to the flood class. These blobs can occur in the midst of a flood, because of fluctuations in the values of the color components (e.g., shadows), disrupting the continuity, and were wrongly classified as background and, therefore, excluded at the early stages of the method.

Figure 8 shows the final segmentation of our proposed approach (see the last column). The blue and dim gray represent the segmented flood and background, respectively. Cyan pixels from the second column, which did not pass the thresholds, and blue pixels, which are not connected to the red ones, are excluded from the segmented flood area. The same applies to the small blue blobs connected to red pixels, because they do not fit the aforementioned area criterion. In the next section, we present more results and discuss them in detail.

## 4. Results and Discussion

In this section, we present our proposed method's results and compare them with selected recent DL approaches, since we did not find any other unsupervised method to challenge this problem. Furthermore, we have conducted an ablation study to measure the contribution of each of our method's modules, as described in Sections 3.2–3.6, with respect to performance.

### 4.1. Evaluation Metrics

The metrics used for evaluation purposes are accuracy ( $ACC$ ), precision ( $PR$ ), recall ( $REC$ ), and F1-score ( $F_1$ ), as defined in Equations (11)–(14) below:

$$ACC = \frac{TP + TN}{TP + TN + FP + FN} \quad (11)$$

$$PR = \frac{TP}{TP + FP} \quad (12)$$

$$REC = \frac{TP}{TP + FN} \quad (13)$$

$$F_1 = \frac{2 \cdot PR \cdot REC}{PR + REC} \quad (14)$$

$TP$ ,  $FP$ ,  $TN$ , and  $FN$  stand for true positive, false positive, true negative, and false negative, respectively. Additionally, we have calculated the average value of the F1-score ( $\bar{F}_1$ ) over the whole dataset, which is given by averaging the corresponding F1-score of each image of the dataset.

### 4.2. Implementation

The proposed method has been implemented using MATLAB 2023b.

All experiments were executed on an Intel I7 CPU processor at 2.3 GHz with 40 GB RAM. The proposed algorithm achieves inference in about half a second per image, without immense calculations that would require the power of GPU cores to perform in the same time range. The proposed method can be easily implemented on a UAV and executed on board due to its low computational and hardware resource requirements.

The code implementing the proposed method, together with the datasets and results, will be publicly available (after acceptance of the article) at the following link (<https://sites.google.com/site/costaspanagiotakis/research/flood-detection> (accessed on 2 May 2024)).

#### 4.3. Flood Area Dataset: Experimental Results and Discussion

We showcase a series of final segmentations as a result of our proposed approach (UFS-HT-REM) supplemented by evaluation metrics, as described above, and the original and ground-truth images. All images have been adjusted to uniform dimensions ( $800 \times 600$ ) for illustration purposes only, since our method works for any image size.

Representative outcomes from the Flood Area dataset are shown in Figures 9–11. The results show flood segmentation in blue overlaid on the original image with the flood's borders emphasized in dark blue. We also use the same technique to represent the ground truth. In Figure 9, the results of the proposed method yield  $F_1$  and  $ACC$  that exceed 90%, showing high-performance results with almost perfect flood detection. In Figure 10,  $F_1$  belongs to the range [75%, 90%], providing results where the flood area detection accuracy is satisfactory. In Figure 11, the results of the proposed method yield  $F_1$  lower than 30%, showing poor segmentation results.

The proposed unsupervised approach works for any tint of flood water and delivers excellent results even when a plethora of small objects protrude the flood, managing to segment around them (see Figures 9b and 10d). As we can observe in the rest of the results, it achieves satisfactory results in urban/peri-urban as well as rural environments, where it accurately segments existing flooded areas, even when they are not labeled in the ground truth, as shown in Figure 10e. The method works best when the acquired image's color quality and the weather and lighting conditions are good, alongside a low camera rotation angle (top-down view). Naturally, should the assumptions underpinning the proposed algorithm not hold, it may result in suboptimal outcomes (see Figure 11). Reasons for bad results include extreme similarity of the flood and the background color, and elevated LAB color components' values of background areas. It is essential that the flood is not green in color, because the vegetation index will confuse it with greenery and, therefore, mainly exclude it (see Figure 11c).

In the LAB colorspace, the flood has been measured to have elevated values with respect to the background. Therefore, in cases when light is reflected on the surface or the sky is of the same brightness, it is impossible for the method to set these two areas apart (see Figure 11a,b). Finally, because the method still relies on color, if there is near-identical coloration of the flood water and other objects (e.g., buildings, rooftops), these objects will be considered part of the flood or will be entirely mistaken as flood, omitting the true flood water (see Figure 11d). High  $ACC$  scores in the poor segmentation results are due to correctly segmenting large areas of the background.



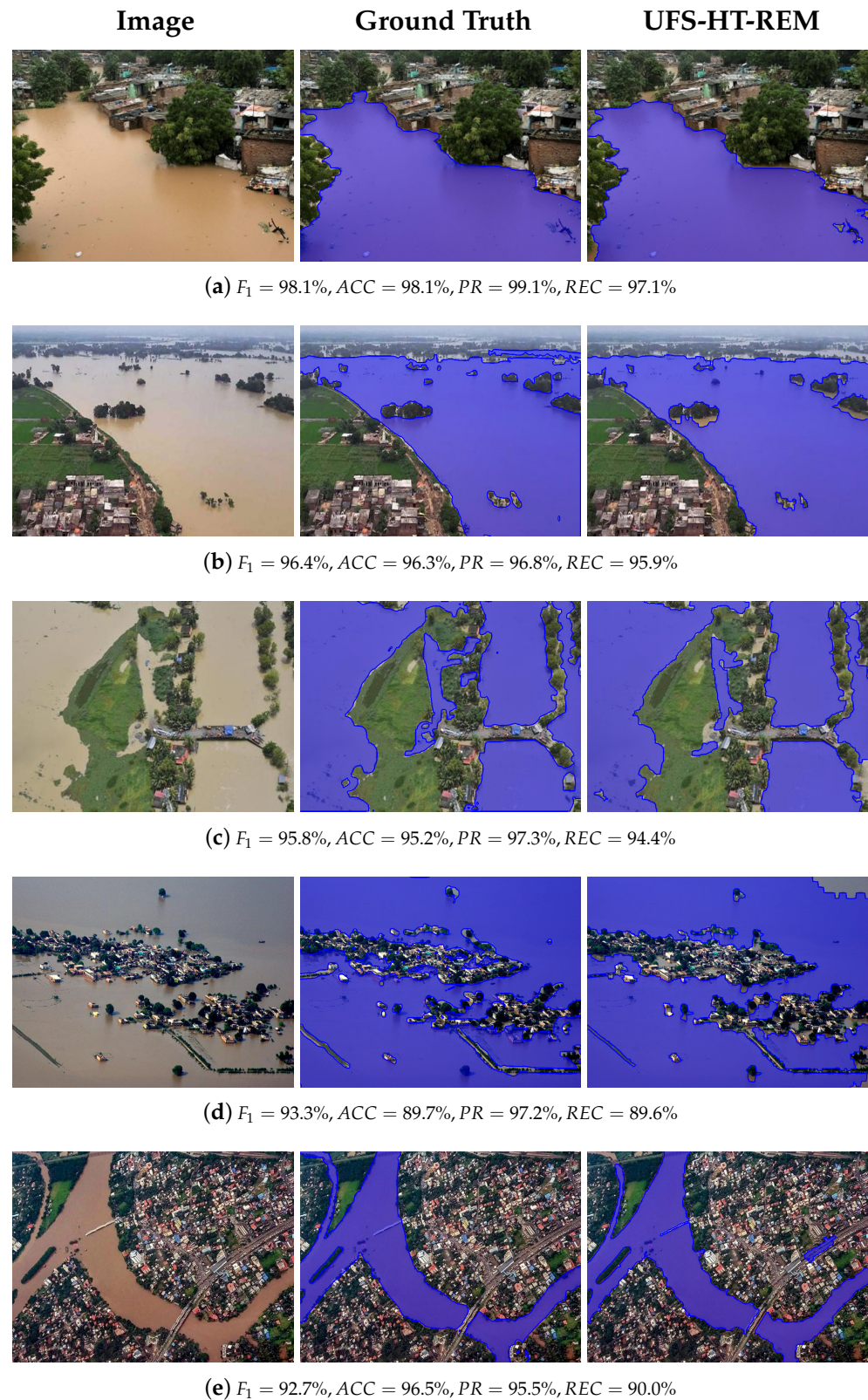


**Figure 9.** High-performance results of the proposed flood segmentation method from the Flood Area dataset. Original images, ground truth, and the final segmentation of our proposed method (UFS-HT-REM).



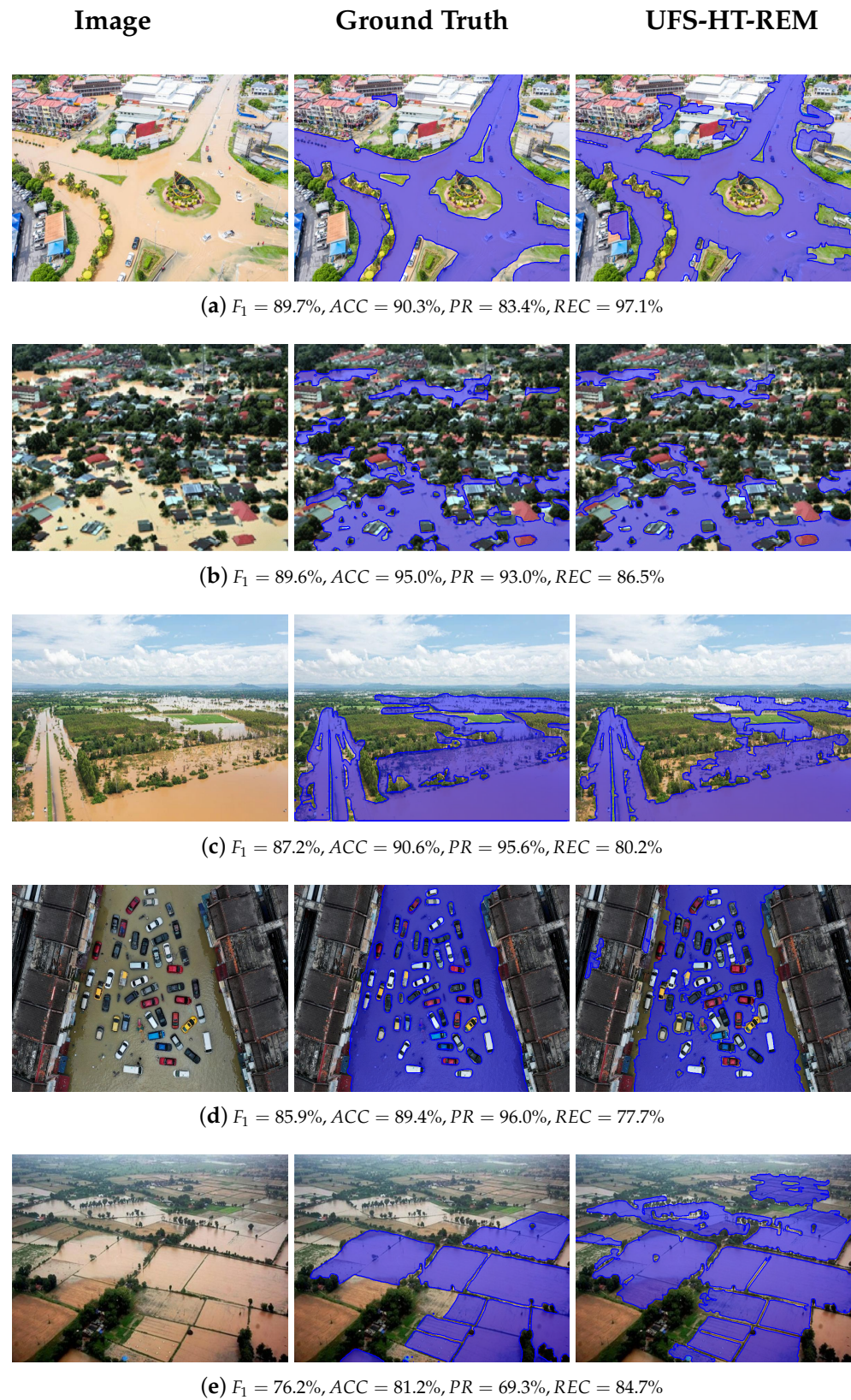


**Figure 10.** Satisfactory results of the proposed flood segmentation method from the Flood Area dataset. Original images, ground truth, and our proposed method's (UFS-HT-REM) final segmentation.

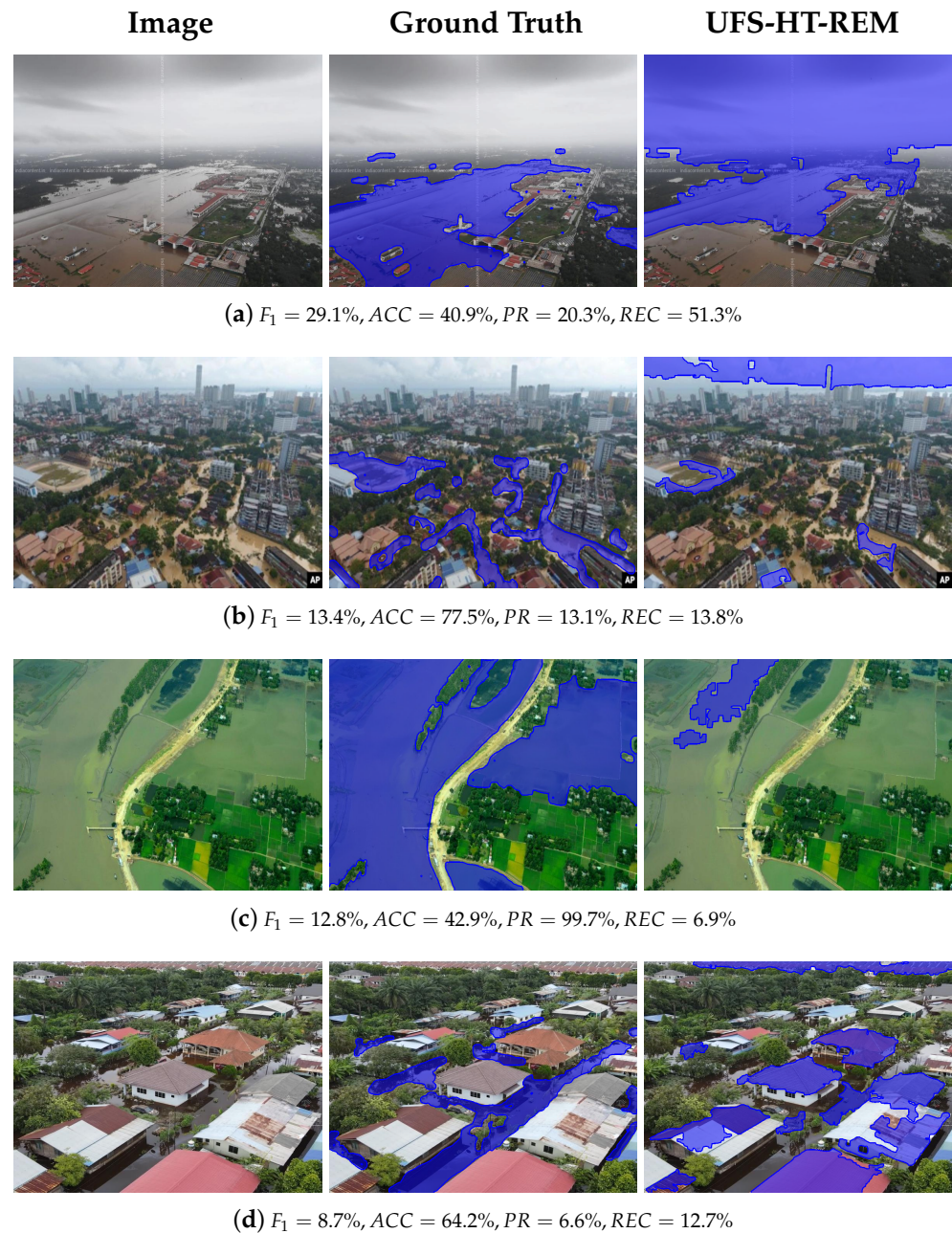


**Figure 11.** Poor segmentations resulting from the proposed methodology (UFS-HT-REM) from the Flood Area dataset. Original images, ground truth, and the final segmentation of our proposed method.

#### 4.4. Exploring the Impact of Environmental Zones and Camera Rotation Angle

Additionally, we study how the environmental zone and the camera rotation angle affect the flooding segmentation by splitting the Flood Area dataset into the following categories:

##### 1. Environmental zone:

- (a) Rural, predominantly featuring fields, hills, rugged mountainsides, scattered housing structures reminiscent of villages or rural settlements, and sparse roads depicted within the images. It consists of 87 out of the 290 images in the dataset.
- (b) Urban and peri-urban, distinctly showcasing urban landscapes characterized by well-defined infrastructure, that conforms to urban planning guidelines; a dense network of roads and high population density reflected in the pres-

ence of numerous buildings and structures. It encompasses a collection of 203 images.

2. Camera rotation angle:

- (a) No sky (almost top-down view, low camera rotation angle), distinguished by the absence of any sky elements; specifically, these images entirely lack any portion of the sky or clouding within their composition. It comprises 182 images of the dataset.
- (b) With sky (bird's-eye view, high camera rotation angle), where elements of the sky, such as clouds or open sky expanses, are visibly present within the image composition. It encompasses the remaining 103 images within the dataset.

This categorization has been undertaken to emphasize that the environment in which the flood is situated can play a role in the final outcome and to encourage further studies to distinguish in their methodologies urban and rural floods, due to their different characteristics.

As we can observe, in the evaluation metrics for these categories, shown in Table 2, our method performs well in all categories. Slightly better results are achieved when the scenery depicts a rural landscape, with  $F_1 = 80.3\%$  being 1.8% higher than in the urban/peri-urban category. The extensive greenery in rural areas allows for the exclusion of a significant number of pixels from PFAs using the RGBVI mask, as described in Section 3.2. However, in the absence of vegetation, the RGBVI does not impact the method's performance, as there will be no greenery to detect. In addition, flooded areas in such environments are usually large in size, which strengthens the dominant color estimation procedure (see Section 3.4), because plentiful pixels are engaged (see category 1.(a) in Table 2). In urbanized areas, the presence of rooftops, buildings and cars, which can have a similar color to flood, leads to mildly decreased performance with  $F_1 = 78.5\%$ , given that parts of these objects are misclassified as flood by the algorithm (see category 1.(b) Table 2).

Furthermore, as we have stated previously, poor segmentation results have been generated when the image featured the sky or parts of the sky. Since the sky's LAB color component values can fall above  $\Delta_C$  (as in Equation (2)), and according to our observation that the flood exhibits higher values in the LAB colorspace, parts of the sky are not excluded from the PFAs in this case. Their pixels are involved in the dominant color estimation and they are commonly segmented as flood. In Table 2, rows 2.(a) and 2.(b) present the evaluation metrics for the categories 'no sky' and 'with sky', with the F1-scores being 79.8% and 77.7%, respectively, in which clearly the 'no sky' group prevails by 2.1%, as expected. This categorization leads to the deduction that when the rotation angle of the UAV's camera is minded, so that the acquired image does not depict any part of the sky but is facing only terrain (a fact that can be controlled by the human operator or the navigation software), the segmentation result is improved.

**Table 2.** Results for the categories of images existing in the Flood Area dataset. The images were divided according to the environmental zone into 1.(a) rural, and 1.(b) urban/peri-urban, and according to the camera rotation angle into 2.(a) no sky (low angle), and 2.(b) with sky (high angle).

Category	ACC	PR	REC	$F_1$	$\overline{F_1}$
1.(a) Rural	83.6%	82.3%	78.4%	80.3%	78.2%
1.(b) Urban/peri-urban	85.4%	78.4%	78.7%	78.5%	76.9%
2.(a) No sky	85.2%	81.6%	78.0%	79.8%	77.9%
2.(b) With sky	84.4%	76.1%	79.5%	77.7%	76.1%
All	84.9%	79.5%	78.6%	79.1%	77.3%



#### 4.5. Ablation Study

The ablation study outlines the significance of each of the proposed method's modules and is reported in Table 3. To do so, we have reported experiments of the proposed method variants, conducted with the Flood Area dataset. The proposed method (UFS-HT-REM) includes all modules and yields the best performance in the following metrics  $ACC = 84.9\%$ ,  $PR = 79.5\%$ ,  $F_1 = 79.1\%$ , and  $\bar{F}_1 = 77.3\%$ .

**Table 3.** Ablation study highlighting the contribution of the method's modules. All experiments were conducted with the Flood Area dataset.

Method	ACC	PR	REC	$F_1$	$\bar{F}_1$
UFS-HT-REM	<b>84.9%</b>	<b>79.5%</b>	78.6%	<b>79.1%</b>	<b>77.3%</b>
UFS-HT-REM (Equation (10))	84.7%	79.2%	78.5%	78.8%	77.0%
UFS-HT-REM (Equation (9))	84.2%	78.6%	78.7%	78.6%	76.7%
UFS-HT	83.4%	76.3%	79.4%	77.8%	75.9%
UFS-REM	82.5%	75.7%	79.1%	77.3%	74.9%
UFS-HT-REM—L	79.9%	68.9%	82.0%	74.8%	72.8%
UFS	78.6%	68.9%	81.1%	74.5%	71.6%
$M_{Final}$ Mask	76.0%	64.9%	82.7%	72.7%	69.8%
UFS-HT-REM—B	74.6%	66.3%	76.1%	70.8%	67.8%
UFS-HT-REM—A	68.6%	56.7%	<b>88.0%</b>	68.9%	66.0%
UFS(Otsu)-HT-REM	72.6%	66.9%	36.8%	47.5%	43.5%

First, we examine the simplification of the probability map (PM) estimation defined in Equation (8), including equally all the LAB color components (UFS-HT-REM Equation (9)) and the AB color components (UFS-HT-REM Equation (10)) for the decisive probability map computation. In both cases, the performance of the method is slightly degraded, since the reduction in  $F_1$  is less than 0.5%. This shows that the proposed Equation (8) is robust and can be replaced by a simpler formula without significant changes. Additionally, it shows that the initialization process is solid, leaving in the PFAs a majority of pixels that are truly flood. From the LAB color components, the luminance  $L$  is of greater importance, as proven by experiments exploiting only one color component:

- $L$  (UFS-HT-REM-L with  $F_1 = 74.8\%$ )
- $A$  (UFS-HT-REM-A with  $F_1 = 68.9\%$ )
- $B$  (UFS-HT-REM-B with  $F_1 = 70.8\%$ )

The core methodology, as described in Sections 3.2–3.4, performs quite adequately (UFS), with the resulting 4.6% lower  $F_1$  compared to UFS-HT-REM. Additionally, by adding the small area removal segment (UFS-REM) or the hysteresis thresholding technique (UFS-HT) separately, performance is improved by about 3% compared to the UFS. It implies that the hysteresis thresholding exerts a slightly better influence, resulting in 0.5% higher  $F_1$  compared to UFS-REM. Overall, each of the proposed components was carefully selected to enhance the final segmentation result.

Finally, the proposed initialization of pixels as potential flood or non-flood using  $\Delta_C$  thresholding (see Equation (2)) is replaced by the Otsu thresholding [46] (UFS(Otsu)-HT-REM), resulting in 31.6% lower  $F_1$  compared to the UFS-HT-REM. This shows that exploiting the standard deviation of the color data relative to their central tendency of the LAB components is a crucial step in the proposed method. This is also proved by the evaluation of the  $M_{Final}$  Mask (see Equation (3)) without any other step of the proposed method, which yields  $F_1 = 72.7\%$ , which is only 6.4% lower compared to the corresponding  $F_1$  of UFS-HT-REM.

To show the stability of the proposed system under different values of system parameters, we performed the following sensitivity test on the two parameters of the hysteresis thresholding technique. Figure 12 depicts the average values of  $ACC$ ,  $REC$ ,  $PR$ , and  $F_1$  computed on the Flood Area dataset for different values of (a)  $T_L$  with  $T_H = 0.75$ , and (b)  $T_H$  with  $T_L = 0.01$ . In any scenario, the method's performance measured with the values of  $F_1$  and  $ACC$  is almost stable, while, as expected, only the values of  $REC$  and  $PR$  slightly decrease and increase, respectively. In conclusion, minor fluctuations in the threshold values do not significantly alter the method's outcome. Although these thresholds are the only parameters that users can modify, they have already been experimentally optimized. Reasonable adjustments to these values produce outcomes that remain nearly identical.

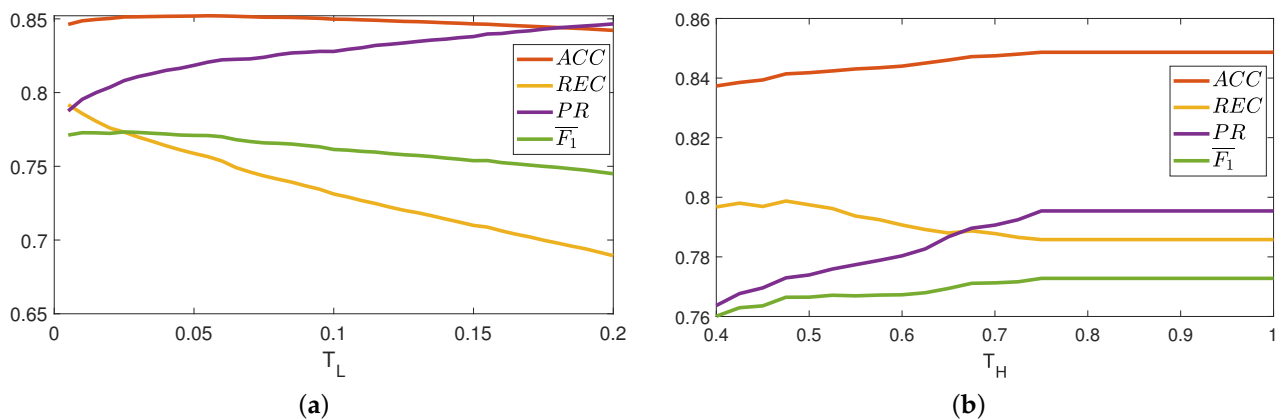


**Figure 12.** The average values of  $ACC$ ,  $REC$ ,  $PR$ ,  $F_1$ , and  $\overline{F_1}$  computed on the Flood Area dataset for different values of (a)  $T_L$  (with  $T_H = 0.75$ ) and (b)  $T_H$  (with  $T_L = 0.01$ ).

#### 4.6. Comparison with DL Approaches

Compared to selected DL approaches, our results are reported in Table 4. We included the best performing FASegNet [19] ( $F_1 = 90.9\%$ ), the intermediate scoring UNet [47] ( $F_1 = 90\%$ ), and the worst performing so far HRNet [48] ( $F_1 = 88.3\%$ ). Although we do not outperform any DL method, UFS-HT-REM scores in close proximity. We are lower by only 3.7% (9.2%) of the HRNet that performs the worst and 6.6% (11.8%) of the FASegNet in accuracy (F1-score), respectively. It is a good compromise taking into account the simplicity of our methodology.

Our method does not require image pre-processing or normalization. The input consists solely of the acquired color image, which can have any resolution and size. In contrast, DL approaches require large training datasets, as well as validation and test sets, and typically necessitate pre-processing and normalization of all input data. Labeling these training and validation sets is time-consuming and prone to human annotation errors. Moreover, data augmentation, essential for training in DL approaches, is unnecessary in our method. Additionally, achieving excellent results with a deep neural network (DNN) trained on one dataset does not guarantee the same performance on a different dataset, often requiring retraining or the use of transfer learning to maintain result quality. Finally, while DL approaches involve thousands to millions of trainable parameters, the proposed method does not involve any.



**Table 4.** Comparison of our proposed approach with selected DL approaches on the Flood Area dataset. The metrics used are accuracy (ACC), precision (PR), recall (REC), and F1-score ( $F_1$ ) (calculated as in Equation (14)) expressed in percentage, and trainable parameters (Tr. Par.) expressed in millions (M).

Method	ACC	PR	REC	$F_1$	Tr. Par.
FASegNet	<b>91.5%</b>	<b>91.4%</b>	90.3%	<b>90.9%</b>	0.64 M
UNet	90.7%	90.0%	90.1%	90.0%	31.05 M
HRNet	88.6%	84.8%	<b>92.0%</b>	88.3%	28.60 M
Ours	84.9%	79.5%	78.6%	79.1%	<b>0 M</b>

#### 4.7. Flood Semantic Segmentation Dataset: Experimental Results and Discussion

To demonstrate the generalization of the proposed algorithm, we used the second dataset, as described in Section 2. It comprises more than twice the number of images compared to the initial one. All images were acquired in diverse real-world scenarios and under different conditions. Without any image pre-processing and modification of the code or parameters, the algorithm performed even higher, reaching 88.5% and 81.7% in accuracy and F1-score, respectively. Consequently, we encountered an increase of 3.6% (2.6%) in ACC ( $F_1$ ). This demonstrates that the observations on which our method is based are universally applicable and resilient. Moreover, it proves that when controllable variables, like the camera's rotation angle, are considered, segmentation outcomes exhibit enhancement, an observation we found to be consistent within this dataset due to the reduced occurrence of sky portions in images. Quantitative metrics in comparison with the first dataset are presented in Table 5. Also, we provide the weighted average in the last row to give an overview of the overall performance of the algorithm in segmenting the flood for 953 images, which depict various scenes and were acquired with different camera settings, e.g., camera rotation angle, focal length, etc.

**Table 5.** Quantitative findings for the Flood Semantic Segmentation dataset (FSSD) in comparison with the Flood Area dataset (FAD) and for the union of the two datasets (calculated as the weighted average due to the varying number of images). The number of images for each dataset (*Images*), accuracy (ACC), precision (PR), recall (REC), and F1-score ( $F_1$ ) (calculated as in Equation (14)) expressed in percentage are reported.

Dataset	Images	ACC	PR	REC	$F_1$	$\bar{F}_1$
FSSD	663	<b>88.5%</b>	<b>79.8%</b>	<b>83.7%</b>	<b>81.7%</b>	<b>79.4%</b>
FAD	290	84.9%	79.5%	78.6%	79.1%	77.3%
FSSD $\cup$ FAD	953	87.4%	79.7%	82.2%	80.9%	78.8%

Representative results for the Flood Semantic Segmentation dataset are shown in Figure 13. Flood segmentation is shown in blue overlaying the original image with the flood's borders emphasized in dark blue. The same technique is used to present the ground truth as well. The best flood segmentation scored 99.6% in  $F_1$ . As we can observe, the excellent segmentations are capable of capturing the flood in its full or almost full extent (Figure 13a,b). Furthermore, high-performing results segment flood details in challenging environments characterized by interference of numerous natural or man-made obstacles (Figure 13c,d). Of course, the same issues leading to poor performance exist, as described in Section 4.3. Figure 13e presents such a low-performance segmentation, where the luminosity of the sky prevents its exclusion from the PFAs. This results in the sky's pixels being assigned significant weights, consequently influencing subsequent probabilities, and ultimately causing them to be misclassified as flood during the hysteresis thresholding isocontour evolution procedure.

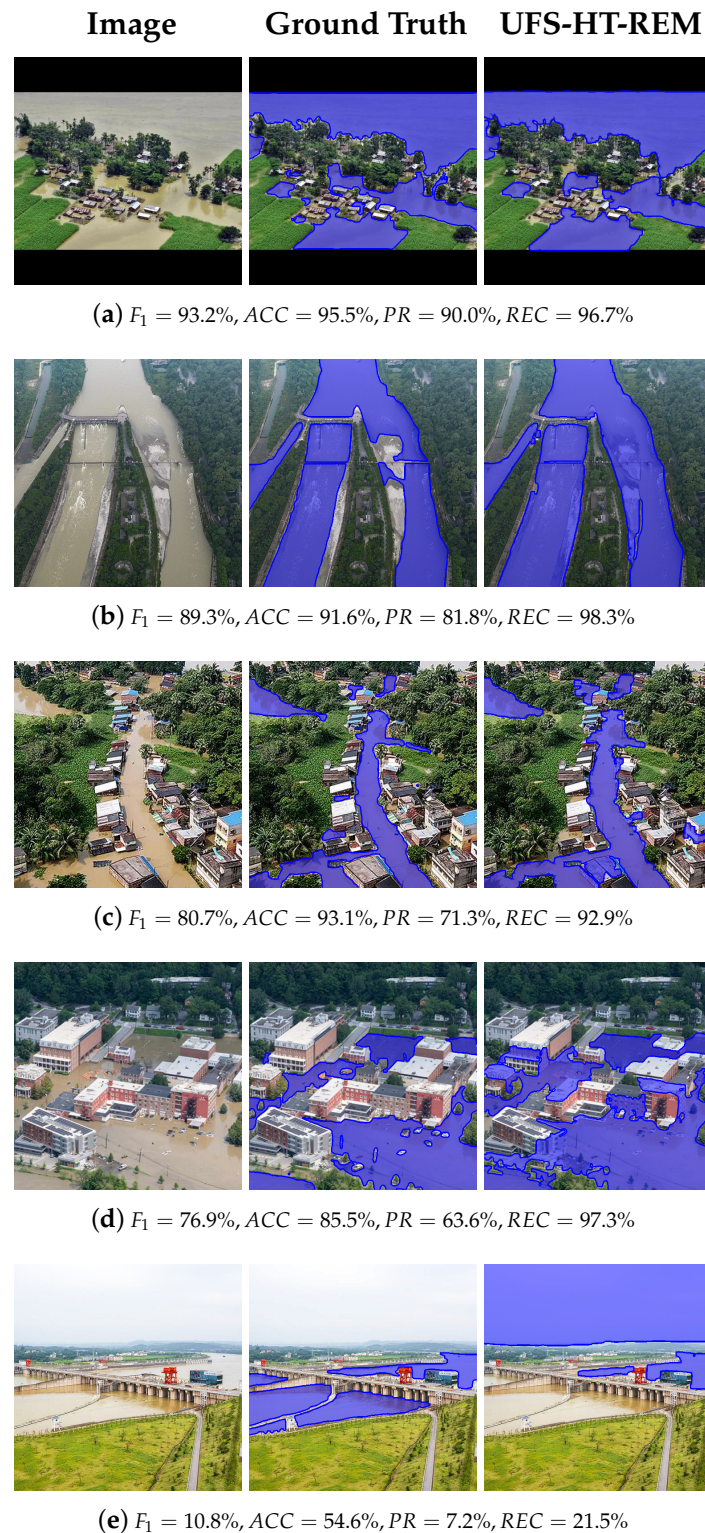


**Figure 13.** Representative results of the proposed methodology (UFS-HT-REM) from the Flood Semantic Segmentation dataset. Original images, ground truth, and the final segmentation of the proposed method are shown from left to right.

## 5. Conclusions and Future Work

Overall, we presented a fully unsupervised approach for flood detection in color images acquired by flying vehicles such as UAVs and helicopters. The method progressively eliminates image regions identified as non-flood using binary masks generated from color

and edge data. Our method operates in a fully unsupervised manner, with no need for training and ground truth labeling. We iteratively apply the same algorithmic steps to each color component. Subsequently, a binary map is generated for each component, discarding regions identified as non-flood and producing a final mask of potential flood areas (PFAs), refined through basic morphological operations. By weighting the pixels within the PFAs, we calculate an estimation of the dominant color of the flood, and a hysteresis thresholding technique is employed to achieve the final segmentation through probabilistic region growing of an isocontour. To the best of our knowledge, it is the first unsupervised approach to tackle this problem.

In this work, we showed that the following simple features suffice to accurately solve the problem of unsupervised flood detection. First of all, the flood's color is similar wherever it appears within the image, and this color differs from the background. Almost always, the flood's color is not green, assuming tree-like vegetation to be covered with water is extreme. Finally, in the LAB colorspace, the flooded area exhibits a higher value in at least one of the color components than the background. The color quality and camera rotation angle of the captured image contribute to the solidity of our observations, and thus a good amount of control over the flying vehicle while capturing the images will support the aforementioned inferences.

To show the robustness of the proposed method, we utilized two datasets containing a total of 953 images, representing diverse real-world areas affected by flood events. All images were acquired by various UAVs operating under different weather conditions and performing a range of flying maneuvers over diverse areas. Our method demonstrated strong generalization to new, unseen data, as it is entirely unsupervised and parameter-free. Since no training is required, all images were exclusively used for testing purposes. Furthermore, we have introduced a categorization of the Flood Area dataset, according to the depicted scenery and camera rotation angle, into rural and urban/per-urban, and no sky and with sky, respectively. We showed that our approach performs well in all categories, slightly excelling in segmenting floods in rural environments and is better suited for acquired images that do not contain sky, which is a controllable factor when maneuvering the UAV. Experimental results confirmed that our proposed approach is robust, performs well in metrics, and is comparable to recent DL approaches, although not outperforming them.

The proposed parameter-free approach is highly efficient, with an inference time of approximately half a second, and does not require image pre-processing or GPU core processing capabilities. This makes the method suitable for on-board execution, allowing real-time flood segmentation to guide relief efforts, thereby preventing loss of life and mitigating the impact of floods on infrastructure. Although the proposed unsupervised method does not outperform any supervised method, it scores in close proximity, being lower by only 6.6% of the best DL method (FASegNet) in accuracy.

In future research, we plan to extend this work by detecting flooded buildings and roads. This will refine existing flood segmentations and correct erroneous segmentations that occur when the observations on which the method relies do not apply to the image. Combined with suitable methodologies which identify buildings and roads, such as Ref. [49], and cross-correlating the results, we will be able to (a) avoid misclassifications of rooftop, building, and road pixels that have a color extremely similar to the flood, thus anticipating attainment of improved outcomes and elevated scores in accurately segmenting the flood event, and (b) identify damaged buildings, when most of their circumference is adjacent to the flood and flooded roads, when there exist discontinuities in the structure. These will help to even better assess the situation in the flood-hit area and more accurately guide disaster assistance, evacuation, and recovery efforts. Additionally, we plan to exploit the knowledge gained in order to construct specialized DL architectures, directing the network's attention towards the flood and even incorporating our classical computer vision approach into hybrid deep learning frameworks tackling the problem.

**Author Contributions:** The authors contributed equally to this work. Conceptualization, G.S. and C.P.; methodology, G.S. and C.P.; software, G.S. and C.P.; validation, G.S. and C.P.; formal analysis, C.P.; investigation, G.S. and C.P.; resources, C.P.; writing—original draft preparation, G.S.; writing—review and editing, G.S. and C.P.; visualization, G.S. and C.P.; supervision, C.P. All authors have read and agreed to the published version of the manuscript.

**Funding:** This research received no external funding.

**Data Availability Statement:** The code implementing the proposed method together with our results and the links to the datasets are publicly available at the following link: <https://sites.google.com/site/costaspanagiotakis/research/flood-detection> (accessed on 2 May 2024).

**Conflicts of Interest:** The authors declare no conflicts of interest.

## Abbreviations

The following abbreviations are used in this manuscript:

ADNet	Attentive Decoder Network
AI	Artificial Intelligence
APLS	Average Path Length Similarity
BCNN	Bayesian Convolutional Neural Network
BiT	Bitemporal image Transformer
CNN	Convolutional Neural Network
CV	Computer Vision
DCFAM	Densely Connected Feature Aggregation Module
DELTA	Deep Earth Learning, Tools, and Analysis
DL	Deep Learning
DNN	Deep Neural Network
DSM	Digital Surface Model
EDN	Encoder–Decoder Network
EDR	Encoder–Decoder Residual
EHAAC	Encoder–Decoder High-Accuracy Activation Cropping
ENet	Efficient Neural Network
HR	High Resolution
ISPRS	International Society for Photogrammetry and Remote Sensing
LSTM	Long Short-Term Memory
ML	Machine Learning
MRF	Markov Random Field
NDWI	Normalized Difference Water Index
PFA	Potential Flood Area
PSPNet	Pyramid Scene Parsing Network
RGBVI	RGB Vegetation Index
ResNet	Residual Network
SAM	Segment Anything Model
SAR	Synthetic Aperture Radar
UAV	Unmanned Aerial Vehicle
VH	Vertical-Horizontal
VV	Vertical-Vertical
WSSS	Weakly Supervised Semantic Segmentation

## References

1. Ritchie, H.; Rosado, P. Natural Disasters. 2022. Available online: <https://ourworldindata.org/natural-disasters> (accessed on 10 May 2024).
2. Kondratyev, K.Y.; Varotsos, C.A.; Krapivin, V.F. *Natural Disasters as Components of Global Ecodynamics*; Springer: Berlin/Heidelberg, Germany, 2006.
3. Algiriyage, N.; Prasanna, R.; Stock, K.; Doyle, E.E.; Johnston, D. Multi-source multimodal data and deep learning for disaster response: A systematic review. *SN Comput. Sci.* **2022**, *3*, 1–29. [CrossRef] [PubMed]
4. Linardos, V.; Drakaki, M.; Tzionas, P.; Karnavas, Y.L. Machine learning in disaster management: Recent developments in methods and applications. *Mach. Learn. Knowl. Extr.* **2022**, *4*, 446–473. [CrossRef]



5. Chouhan, A.; Chutia, D.; Aggarwal, S.P. Attentive decoder network for flood analysis using sentinel 1 images. In Proceedings of the 2023 International Conference on Communication, Circuits, and Systems (IC3S), Bhubaneswar, India, 26–28 May 2023; IEEE: Piscataway, NJ, USA, 2023; pp. 1–5.
6. Drakonakis, G.I.; Tsagkatakis, G.; Fotiadou, K.; Tsakalides, P. OmbriaNet—Supervised flood mapping via convolutional neural networks using multitemporal sentinel-1 and sentinel-2 data fusion. *IEEE J. Sel. Top. Appl. Earth Obs. Remote Sens.* **2022**, *15*, 2341–2356. [\[CrossRef\]](#)
7. Dong, Z.; Liang, Z.; Wang, G.; Amankwah, S.O.Y.; Feng, D.; Wei, X.; Duan, Z. Mapping inundation extents in Poyang Lake area using Sentinel-1 data and transformer-based change detection method. *J. Hydrol.* **2023**, *620*, 129455. [\[CrossRef\]](#)
8. Hänsch, R.; Arndt, J.; Lunga, D.; Gibb, M.; Pedelose, T.; Boedihardjo, A.; Petrie, D.; Bacastow, T.M. Spacenet 8-the detection of flooded roads and buildings. In Proceedings of the IEEE/CVF Conference on Computer Vision and Pattern Recognition, New Orleans, LA, USA, 19–20 June 2022; pp. 1472–1480.
9. He, Y.; Wang, J.; Zhang, Y.; Liao, C. An efficient urban flood mapping framework towards disaster response driven by weakly supervised semantic segmentation with decoupled training samples. *ISPRS J. Photogramm. Remote Sens.* **2024**, *207*, 338–358. [\[CrossRef\]](#)
10. Hernández, D.; Cecilia, J.M.; Cano, J.C.; Calafate, C.T. Flood detection using real-time image segmentation from unmanned aerial vehicles on edge-computing platform. *Remote Sens.* **2022**, *14*, 223. [\[CrossRef\]](#)
11. Hertel, V.; Chow, C.; Wani, O.; Wieland, M.; Martinis, S. Probabilistic SAR-based water segmentation with adapted Bayesian convolutional neural network. *Remote Sens. Environ.* **2023**, *285*, 113388. [\[CrossRef\]](#)
12. Ibrahim, N.; Sharun, S.; Osman, M.; Mohamed, S.; Abdullah, S. The application of UAV images in flood detection using image segmentation techniques. *Indones. J. Electr. Eng. Comput. Sci.* **2021**, *23*, 1219. [\[CrossRef\]](#)
13. Inthizami, N.S.; Ma'sum, M.A.; Alhamidi, M.R.; Gamal, A.; Ardianto, R.; Jatmiko, W.; Kurnianingsih. Flood video segmentation on remotely sensed UAV using improved Efficient Neural Network. *ICT Express* **2022**, *8*, 347–351. [\[CrossRef\]](#)
14. Li, Z.; Demir, I. U-net-based semantic classification for flood extent extraction using SAR imagery and GEE platform: A case study for 2019 central US flooding. *Sci. Total. Environ.* **2023**, *869*, 161757. [\[CrossRef\]](#)
15. Lo, S.W.; Wu, J.H.; Lin, F.P.; Hsu, C.H. Cyber surveillance for flood disasters. *Sensors* **2015**, *15*, 2369–2387. [\[CrossRef\]](#) [\[PubMed\]](#)
16. Munawar, H.S.; Ullah, F.; Qayyum, S.; Heravi, A. Application of deep learning on uav-based aerial images for flood detection. *Smart Cities* **2021**, *4*, 1220–1242. [\[CrossRef\]](#)
17. Park, J.C.; Kim, D.G.; Yang, J.R.; Kang, K.S. Transformer-Based Flood Detection Using Multiclass Segmentation. In Proceedings of the 2023 IEEE International Conference on Big Data and Smart Computing (BigComp), Jeju, Republic of Korea, 13–16 February 2023; IEEE: Piscataway, NJ, USA, 2023; pp. 291–292.
18. Rahneemoonfar, M.; Chowdhury, T.; Sarkar, A.; Varshney, D.; Yari, M.; Murphy, R.R. Floodnet: A high resolution aerial imagery dataset for post flood scene understanding. *IEEE Access* **2021**, *9*, 89644–89654. [\[CrossRef\]](#)
19. Şener, A.; Doğan, G.; Ergen, B. A novel convolutional neural network model with hybrid attentional atrous convolution module for detecting the areas affected by the flood. *Earth Sci. Inform.* **2024**, *17*, 193–209. [\[CrossRef\]](#)
20. Shastry, A.; Carter, E.; Coltin, B.; Sleeter, R.; McMichael, S.; Eggleston, J. Mapping floods from remote sensing data and quantifying the effects of surface obstruction by clouds and vegetation. *Remote Sens. Environ.* **2023**, *291*, 113556. [\[CrossRef\]](#)
21. Wang, L.; Li, R.; Duan, C.; Zhang, C.; Meng, X.; Fang, S. A novel transformer based semantic segmentation scheme for fine-resolution remote sensing images. *IEEE Geosci. Remote Sens. Lett.* **2022**, *19*, 1–5. [\[CrossRef\]](#)
22. Wieland, M.; Martinis, S.; Kiefl, R.; Gstaiger, V. Semantic segmentation of water bodies in very high-resolution satellite and aerial images. *Remote Sens. Environ.* **2023**, *287*, 113452. [\[CrossRef\]](#)
23. Bauer-Marschallinger, B.; Cao, S.; Tupas, M.E.; Roth, F.; Navacchi, C.; Melzer, T.; Freeman, V.; Wagner, W. Satellite-Based Flood Mapping through Bayesian Inference from a Sentinel-1 SAR Datacube. *Remote Sens.* **2022**, *14*, 3673. [\[CrossRef\]](#)
24. Filonenko, A.; Hernández, D.C.; Seo, D.; Jo, K.H. Real-time flood detection for video surveillance. In Proceedings of the IECON 2015-41st Annual Conference of the IEEE Industrial Electronics Society, Yokohama, Japan, 9–12 November 2015; IEEE: Piscataway, NJ, USA, 2015; pp. 004082–004085.
25. Landuyt, L.; Verhoest, N.E.; Van Coillie, F.M. Flood mapping in vegetated areas using an unsupervised clustering approach on sentinel-1 and-2 imagery. *Remote Sens.* **2020**, *12*, 3611. [\[CrossRef\]](#)
26. McCormack, T.; Campaña, J.; Naughton, O. A methodology for mapping annual flood extent using multi-temporal Sentinel-1 imagery. *Remote Sens. Environ.* **2022**, *282*, 113273. [\[CrossRef\]](#)
27. Trombini, M.; Solarna, D.; Moser, G.; Dellepiane, S. A goal-driven unsupervised image segmentation method combining graph-based processing and Markov random fields. *Pattern Recognit.* **2023**, *134*, 109082. [\[CrossRef\]](#)
28. Bentivoglio, R.; Isufi, E.; Jonkman, S.N.; Taormina, R. Deep learning methods for flood mapping: A review of existing applications and future research directions. *Hydrol. Earth Syst. Sci.* **2022**, *26*, 4345–4378. [\[CrossRef\]](#)
29. Kumar, V.; Azamathulla, H.M.; Sharma, K.V.; Mehta, D.J.; Maharaj, K.T. The state of the art in deep learning applications, challenges, and future prospects: A comprehensive review of flood forecasting and management. *Sustainability* **2023**, *15*, 10543. [\[CrossRef\]](#)
30. Yu, F.; Koltun, V. Multi-Scale Context Aggregation by Dilated Convolutions. *arXiv* **2016**, arXiv:1511.07122.
31. Kirillov, A.; Mintun, E.; Ravi, N.; Mao, H.; Rolland, C.; Gustafson, L.; Xiao, T.; Whitehead, S.; Berg, A.C.; Lo, W.Y.; et al. Segment Anything. *arXiv* **2023**, arXiv:2304.02643.

32. Tarpanelli, A.; Mondini, A.C.; Camici, S. Effectiveness of Sentinel-1 and Sentinel-2 for flood detection assessment in Europe. *Nat. Hazards Earth Syst. Sci.* **2022**, *22*, 2473–2489. [\[CrossRef\]](#)
33. Guo, Z.; Wu, L.; Huang, Y.; Guo, Z.; Zhao, J.; Li, N. Water-body segmentation for SAR images: Past, current, and future. *Remote Sens.* **2022**, *14*, 1752. [\[CrossRef\]](#)
34. O'Mahony, N.; Campbell, S.; Carvalho, A.; Harapanahalli, S.; Hernandez, G.V.; Krpalkova, L.; Riordan, D.; Walsh, J. Deep learning vs. traditional computer vision. In Proceedings of the Advances in Computer Vision: Proceedings of the 2019 Computer Vision Conference (CVC), Las Vegas, NV, USA, 2–3 May 2019; Springer: Berlin/Heidelberg, Germany, 2020; Volume 2, pp. 128–144.
35. Karim, F.; Sharma, K.; Barman, N.R. Flood Area Segmentation. Available online: <https://www.kaggle.com/datasets/faizalkarim/flood-area-segmentation> (accessed on 10 May 2024).
36. Yang, L. Flood Semantic Segmentation Dataset. Available online: <https://www.kaggle.com/datasets/lihuayang111265/flood-semantic-segmentation-dataset> (accessed on 10 May 2024).
37. Bendig, J.; Yu, K.; Aasen, H.; Bolten, A.; Bennertz, S.; Broscheit, J.; Gnyp, M.L.; Bareth, G. Combining UAV-based plant height from crop surface models, visible, and near infrared vegetation indices for biomass monitoring in barley. *Int. J. Appl. Earth Obs. Geoinf.* **2015**, *39*, 79–87. [\[CrossRef\]](#)
38. Markaki, S.; Panagiotakis, C. Unsupervised Tree Detection and Counting via Region-Based Circle Fitting. In Proceedings of the ICPRAM, Lisbon, Portugal, 22–24 February 2023; pp. 95–106.
39. Ashapure, A.; Jung, J.; Chang, A.; Oh, S.; Maeda, M.; Landivar, J. A comparative study of RGB and multispectral sensor-based cotton canopy cover modelling using multi-temporal UAS data. *Remote Sens.* **2019**, *11*, 2757. [\[CrossRef\]](#)
40. Chavolla, E.; Zaldivar, D.; Cuevas, E.; Perez, M.A. Color spaces advantages and disadvantages in image color clustering segmentation. In *Advances in Soft Computing and Machine Learning in Image Processing*; Springer: Berlin/Heidelberg, Germany, 2018; pp. 3–22.
41. Hernandez-Lopez, J.J.; Quintanilla-Olvera, A.L.; López-Ramírez, J.L.; Rangel-Butanda, F.J.; Ibarra-Manzano, M.A.; Almanza-Ojeda, D.L. Detecting objects using color and depth segmentation with Kinect sensor. *Procedia Technol.* **2012**, *3*, 196–204. [\[CrossRef\]](#)
42. Colorimetry—Part 4: CIE 1976 L\*a\*b\* Colour Space. Available online: <https://cie.co.at/publications/colorimetry-part-4-cie-1976-lab-colour-space-0> (accessed on 10 May 2024).
43. Gonzalez, R.C.; Woods, R.E. *Digital Image Processing*, 4th ed.; Global Edition; Pearson: London, UK, 2018; pp. 405–420.
44. Canny, J. A computational approach to edge detection. *IEEE Trans. Pattern Anal. Mach. Intell.* **1986**, *PAMI-8*, 679–698.
45. Fabbri, R.; Costa, L.D.F.; Torelli, J.C.; Bruno, O.M. 2D Euclidean distance transform algorithms: A comparative survey. *ACM Comput. Surv. (CSUR)* **2008**, *40*, 1–44. [\[CrossRef\]](#)
46. Xu, X.; Xu, S.; Jin, L.; Song, E. Characteristic analysis of Otsu threshold and its applications. *Pattern Recognit. Lett.* **2011**, *32*, 956–961. [\[CrossRef\]](#)
47. Ronneberger, O.; Fischer, P.; Brox, T. U-net: Convolutional networks for biomedical image segmentation. In Proceedings of the Medical Image Computing and Computer-Assisted Intervention—MICCAI 2015: 18th International Conference, Munich, Germany, 5–9 October 2015; Proceedings, Part III 18; Springer: Berlin/Heidelberg, Germany, 2015; pp. 234–241.
48. Sun, K.; Xiao, B.; Liu, D.; Wang, J. Deep high-resolution representation learning for human pose estimation. In Proceedings of the IEEE/CVF Conference On Computer Vision and Pattern Recognition, Long Beach, CA, USA, 15–20 June 2019; pp. 5693–5703.
49. Grinias, I.; Panagiotakis, C.; Tziritas, G. MRF-based segmentation and unsupervised classification for building and road detection in peri-urban areas of high-resolution satellite images. *ISPRS J. Photogramm. Remote Sens.* **2016**, *122*, 145–166. [\[CrossRef\]](#)

**Disclaimer/Publisher's Note:** The statements, opinions and data contained in all publications are solely those of the individual author(s) and contributor(s) and not of MDPI and/or the editor(s). MDPI and/or the editor(s) disclaim responsibility for any injury to people or property resulting from any ideas, methods, instructions or products referred to in the content.